PARAMETER ESTIMATION AND DETECTION OF GRAVITATIONAL WAVES USING PARTICLE SWARM ALGORITHM

A Thesis

submitted to
Indian Institute of Science Education and Research Pune
in partial fulfillment of the requirements for the
BS-MS Dual Degree Programme

by

Varun Srivastava
20121026

Indian Institute of Science Education and Research Pune
Dr. Homi Bhabha Road,
Pashan, Pune 411008, INDIA.

May, 2017

Supervisor: Dr. Sukanta Bose

Certificate

This is to certify that this dissertation entitled PARAMETER ESTIMATION AND DETECTION OF GRAVITATIONAL WAVES USING PARTICLE SWARM ALGORITHM towards the partial fulfilment of the BS-MS dual degree programme at the Indian Institute of Science Education and Research, Pune represents study/work carried out by Varun Srivastava at Inter-University Centre for Astronomy and Astrophysics, Pune under the supervision of Dr. Sukanta Bose, Professor, Department of Physics Inter-University Centre for Astronomy and Astrophysics, Pune during the academic year 2016-2017.

Dr. Sukanta Bose
IUCAA, Pune.

(30 March 2017)
Varun Srivastava
IISER, Pune.

Committee:

Dr. Sukanta Bose

Dr. Prasad Subhramanian

Dedicated to my adorable sister
Vini.

Declaration

I hereby declare that the matter embodied in the report entitled PARAMETER ESTIMATION AND DETECTION OF GRAVITATIONAL WAVES USING PARTICLE SWARM ALGORITHM are the results of the work carried out by me at the Department of Physics, Inter-University Centre for Astronomy and Astrophysics, Pune under the supervision of Dr. Sukanta Bose and the same has not been submitted elsewhere for any other degree.

(30 March, 2017)
Varun Srivastava
IISER, Pune.

Dr. Sukanta Bose
IUCAA, Pune.

Acknowledgments

I am thankful to Dr. Sukanta Bose for being my project supervisor. Your guidance, mentorship, and motivation drove me to complete each project I undertook. Your foresight into any project, the ideas to coherently build it and the take away for future studies approach is what I aspire to develop during my course of advance study.

I am deeply grateful to Dr. Rajesh Nayak guidance, constructive ideas and valuable discussions, lead to the completion of my project on PSO project. I thank you very much for your patience in clearing my doubts, for being my mentor and counselor. Thank you so much for your motivation to be persistent in my attempts.

My sincere thanks to Dr. Varun Bhalerao who not only guided me through the projects but has been a great mentor, teacher and friend. Thank you for your guidance which lead to the completion of our project on geographic dependencies. I have learned a wide range of essential research skills from you. I have enjoyed my first hands experience on writing research papers and being a corresponding author. I also thank Reed Essick, Leo Singer and Archisman Ghosh for helpful discussions.

I am in debt to Bhushan Gadre. Without your help, my project would not have moved forward. Thank you for solving my day to day code problems, clearing my misconceptions, in software installation and leaking top secret guidelines on how to use pycbc packages. I am also thankful to Javed Rana for the help on using different astronomy software.

I am thankful to Dr. Jayanti Prasad for his help with the IUCAA grid services and the Sarathi cluster at IUCAA which supported the computational work for the present study.

I thank Dr. Prasad Subramanian for being my local mentor at IISER Pune and offering assistance in every form. I would like to thank my parents for their motivation. My group at IUCAA Anir-

ban Ain and Anuradha Gupta for intellectual discussions. My friends at IISER Abhishek Anand, Abhijit Fulkar, Irene Dutta, Kunal Mozumdar, Omkar Manjerekar and Vished Kumar who have helped me to both relax and regain focus.

Abstract

We explore the possibility to detect gravitational waves buried in the data stream of gravitational wave detectors, like Laser Interferometer Gravitational wave Observatory (LIGO), using the particle swarm optimization (PSO) algorithm. Our results show that PSO is a powerful tool to detect gravitational waves and as well as estimate source parameters to reasonable accuracy at much lower computational cost. We also shed light on a variant of PSO developed during the course of our project. We also present results for another study which aims to investigate geographical factors and annual timing of LIGO-VIRGO science runs, on the probability of finding electromagnetic counterparts of an astrophysical gravitational wave source.

Contents

Abstract **xi**

1 Introduction **7**
1.1 General theory of Relativity . . . 7
1.2 Gravitational Waves . . . 9
1.3 Quadrupole approximation . . . 12
1.4 Astrophysical Sources of Gravitational Waves . . . 13
1.5 Electromagnetic Counterparts . . . 15

2 Detecting Gravitational Waves **17**
2.1 Laser Interferometer based Gravitational Wave Detector . . . 18
2.2 Sources of Noise . . . 21
2.3 Gravitational Wave Data Analysis . . . 24

3 Particle Swarm Optimization **31**
3.1 Particle Swarm Algorithm . . . 31
3.2 Multi-Swarm Optimization . . . 34
3.3 Hostile Particle Swarm . . . 34
3.4 Applications . . . 38
3.5 Discussions . . . 46

4 Detecting Gravitational waves using PSO **47**
4.1 Approach . . . 48
4.2 Variants of PSO . . . 49
4.3 Boundary Conditions . . . 50
4.4 Results and Discussion . . . 52
4.5 Future Work . . . 56

5 Geographic and Annual Influences on Optical Followup of Gravitational Wave Events **61**
5.1 Method . . . 62
5.2 Observing on Solstices and Equinoxes . . . 67
5.3 LIGO-VIRGO Science Runs . . . 70

5.4 Discussion 71

List of Figures

1.1 The two frames shown in the figure are equivalent according to the principle of equivalence. The photon as it travels across the spaceship moving upwards with an acceleration of a will exit the spaceship at a point lower than its entry as depicted in the figure. This frame is equivalent to a frame with a gravitational potential of a. Thus, the photon path should bend due to the gravitational potential as depicted in the figure on the right. 8

1.2 The effect of the two polarizations (h_+ and $h_\times$) of GWs on a ring of test mass particles. The figure shows how the ring is distorted over time due to the passage of purely polarized GWs. 11

1.3 Different sources of GWs, categorized by the frequency of the emitted GWs are summarized in the figure above. The detectors which are capable of detecting the respective GW source in a given frequency bin are shown below. *Courtesy:* "Gravitational Astrophysics Laboratory". `science.gsfc/nasa.gov` 14

1.4 The EM counterparts of a NS-NS/NS-BH merger are summarized in the figure above. We see that the signal is distributed over the entire range of the EM spectrum – Gamma ray burst, Optical-Infrared and Radio. [1] 15

2.1 The schematic diagram of the LIGO interferometers. [2] 18

2.2 The figure shows the schematic layout of the Michelson interferometer. 19

2.3 The figure depicts a Fabry-Perot cavity. The mirror reflectivity and transmittance are represented by r and t respectively. The intensity of the incoming beam is E_0. 19

2.4 The figure summarizes the different noise sources which limit the advanced-LIGO detector sensitivity over the range of frequency. [3] 22

2.5 Location of the GW detectors across the globe. 23

2.6 The figure shows a typical GW waveform due to compact binary coalesce. The above waveform arises from to the coalesce of a 35-30 $M_\odot$. The green, yellow and pink regions respectively represent the inspiral, merger and ringdown phases of the evolution of the binary system. 25

3.1 At any instant of time, the factors which influence the velocity of a particle in PSO. 33

3.2 A schematic diagram illustrating the hostile swarm variant of PSO. 35

3.3 The distance constraint around the global best will carve out the area shaded in green from the parameter space. In doing so, the location where line cuts the curve becomes a fictitious peak arising due to the constraint. 37
3.4 The plot shows the particles in a sub-swarm fail to converge due to the effect of the repulsion potential. The particles tend to drift away from the optimal location due to the repulsion force from the other sub-swarm. 37
3.5 The figure shows that the performance of the hostile swarms is independent of the ratio of split of particles in the primary and secondary swarm. The simulation presented uses hostile swarms with an electrostatic repulsion potential between the sub-swarms to search an eight-dimensional parameter space with a total of 2400 particles. 39
3.6 Simulations with a linear repulsion potential between sub-swarms while searching an eight-dimensional parameter space with 2400 particle. We see linear repulsion potential is a poor choice for higher dimensional spaces. 41
3.7 A comparison of the possible search methods with hostile swarms in an eight-dimensional search space. A total of 2400 particles are equally distributed between the two sub-swarms of hostile nature simulated by an electrostatic repulsion potential. 43
3.8 Comparing the performance of hostile swarm technique (after removing, if any, recurrent solution in a given trial) with PSO. We see with hostile swarm method provides an increased efficiency of exploring both the global and local optimal solutions. 45

4.1 The figure shows the average change in global best location averaged over 1000 trials as a function of time. We see in later iterations the global best barely changes. 49
4.2 Comparing different variants of PSO (using a total of 400 particles) from their efficiency to estimate source parameters from likelihood optimization to recover high-spin BH-BH injections. 53
4.3 Comparing different variants of PSO (using a total of 400 particles) from their efficiency to estimate source parameters from likelihood optimization to recover low-spin BH-BH injections. 54
4.4 Comparing different variants of PSO (using a total of 600 particles) from their efficiency to estimate source parameters from likelihood optimization to recover low-spin NS-NS/NS-BH injections. 57
4.5 Comparing different variants of PSO (using a total of 600 particles) from their efficiency to estimate source parameters from matched filter optimization to recover low-spin NS-NS/NS-BH injections. 58
4.6 Comparing different variants of PSO (using a total of 600 particles) from their efficiency to estimate source parameters from matched filter optimization to recover high-spin NS-NS/NS-BH injections. 59
4.7 Estimation of χ_{eff} 60

5.1 Using the time of arrival information to localize the source in the sky, the blue ellipses represent the 90% localization area in the sky. The red crosses are the blind spots of the detector network. The plot uses the O2 (2017-2018) detector sensitivity to localize the sources in the sky. [4] 62
5.2 The locations of the Optical-Infrared ground-based observatories which took part in the EM-followup of GW150914 event. We have added Hanle as a representative observatory in Asia. 63
5.3 A box and whiskers plot for a given histogram plot. 67
5.4 Comparing the performance of three locations – La Serena, Hanle and Palomar, after shifting all the injections recovered with a two detector network to the day of vernal equinox (green), summer solstice (yellow), autumn equinox (chocolate) and winter equinox (blue). 68
5.5 We plot the median probability covered by any location when all the injections recovered with a two detector network (left) and with a three detector network (right) are shifted to the day of the vernal equinox (green), summer solstice (yellow), autumn equinox (chocolate) and winter equinox (blue). We see a trend in the median probability covered as a function of the latitude. 68
5.6 The figure compares the location wise performance of all locations when all 1024 events recovered with a two detector network are shifted to the day of the autumn equinox. We see all locations perform comparable with a slight trend in latitude. . 69
5.7 Distribution of probability covered when each location is equipped with a 30 sq. deg. coverage capability. We see the performance is limited by the patch visibility and access from any given location as we have a large number of triggers which are covered almost completely $p_{obs} > 0.95$ while other triggers are barely followed-up $p_{obs} < 0.05$. 71
5.8 Location wise performance for 630 events recovered at O1 detector sensitivity during the O1 observational period. 72
5.9 Location wise performance for 394 events recovered at O2 detector sensitivity, with events uniformly distributed over the example O2 observational period. 73
5.10 Location wise performance for all the events recovered with a three detector network at O2 detector sensitivity. The events are uniformly smeared over the example O2B observational period. 74

List of Tables

3.1 The table summarizes the total number of particles used to sample the parameter space in N dimension. The boundaries are defined at (-5, 5) along any dimensional axis. 40

4.1 Injection parameters in different search categories. All the signals which are injected have a SNR $\geq$ 8. 48

4.2 Detection efficiency and errors in source parameter estimation for different boundary conditions used, when all the 1000 injections are forced near the boundary. All the signals are injected with an SNR $\geq$ 8. The table summarizes the mean and standard deviation in the error estimation of the parameters – chirp mass, the mass ratio and effective spin parameters. 51

4.3 Detection efficiency and errors in source parameter estimation for different boundary conditions used, when the 1000 injections are uniformly smeared in the parameter space defined in the low-Spin BH-BH binaries category in table 4.1. All the signals are injected with an SNR $\geq$ 8. The table summarizes the mean and standard deviation in the error estimation of the parameters – chirp mass, the mass ratio and effective spin parameters. 52

4.4 The table summarized the detection efficiency of different variants of PSO surveyed. The search is done using the likelihood function as the fitness function. All the signals are injected with an SNR $\geq$ 8. 55

4.5 The table summarized the detection efficiency of different variants of PSO surveyed. All the signals are injected with an SNR $\geq$ 8. 56

5.1 Details of observatory locations that took part in the follow-up of GW150914 event. 65

Chapter 1

Introduction

1.1 General theory of Relativity

The general theory of relativity was proposed by Einstein in 1915. Newton's theory of gravity does not address a fundamental question – the speed with which gravitational force propagates. Implying, that any changes in mass distribution locally would result in changes everywhere in the universe instantaneous. The following idea is in direct conflict with Einstein's special relativity which allows that information can not propagate faster than the speed of light c. This fundamental flaw motivated Einstein to develop a new theory of gravity.

To address the above question, Einstein used the principle of equivalence which later served as the cornerstone to the theory's mathematical formulation. The hypothesis is that reference frames with a uniform gravitational field (like earth) are equivalent to frames which are accelerating with respect to an inertial reference frame (a freely falling elevator). The very assumption gives rise to the prediction that gravitational fields should bend the path of photon (discussed later). Eddington in 1919 proved this prediction showing light from distant star bends due to the gravitational field of the sun. Over a century, the general theory of relativity has been extensively tested, the experimental results making a peaceful agreement with the theory each time. One of the last of the untested theory prediction – the existence of gravitational waves (GW), was verified by LIGO in the landmark discovery of February 2016 [5, 6]. We will briefly discuss the mathematical formulation and the consequences of this theory which has revolutionized modern physics and cosmology.

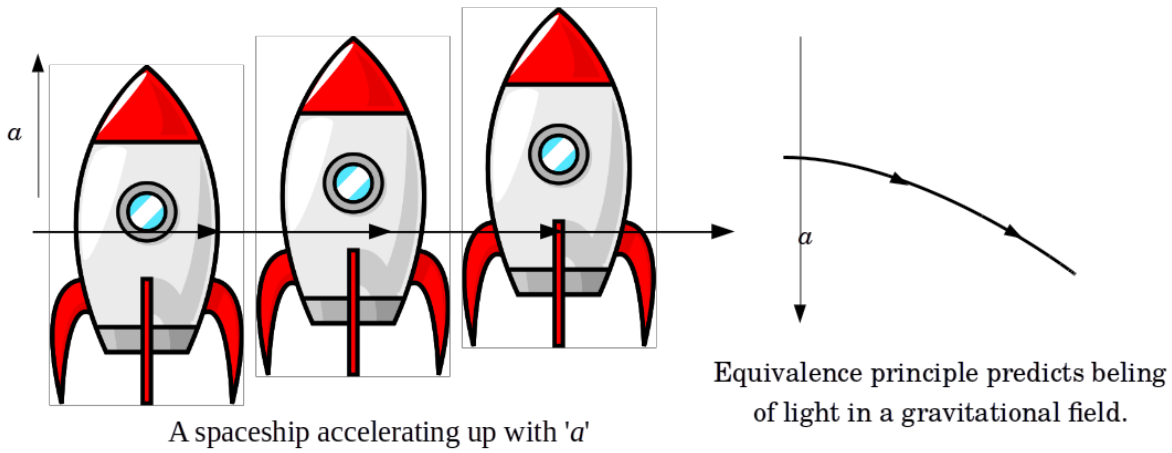

Figure 1.1: The two frames shown in the figure are equivalent according to the principle of equivalence. The photon as it travels across the spaceship moving upwards with an acceleration of a will exit the spaceship at a point lower than its entry as depicted in the figure. This frame is equivalent to a frame with a gravitational potential of a. Thus, the photon path should bend due to the gravitational potential as depicted in the figure on the right.

As stated, equivalence principle predicts the bending of light as it traverses through a gravitational potential due to a massive object. Another important consequence which seeds from the same principle are the gravitational red-shift – photons traveling into a gravitational potential (in GR it's more meaningful to use curvature) is blue-shifted and vice-verse, gravitational time dilation – time runs slower for an object with higher curvature (gravitational potential). How and why does curvature come into the picture?

Uniform gravitational fields are equivalent to frames which are accelerating with respect to an inertial reference frame. Let us consider an elevator moving upwards with a constant acceleration with respect to an inertial reference frame. A photon enters from the left, the trajectory of the photon as seen from the inertial frame is shown in figure 1.1. Using equivalence principle, the elevator frame is equivalent to a uniform gravitational field. Thus, photons or test masses bend in the presence of a uniform gravitational field. To describe these trajectories, called geodesics, Einstein used manifolds and curvatures.

In Einstein's special theory of relativity, mass, energy, and momentum are interchangeable. Thus, in general theory of relativity unlike Newton's theory of gravity – not just mass but the distribution of energy and momentum which can give rise to gravitational fields. This information is

incorporated in the 4X4 energy momentum tensor $T_{\alpha\beta}$ [7]. The Einstein's equations are:

$$G_{\alpha\beta} = R_{\alpha\beta} - \frac{1}{2}g_{\alpha\beta}R = \frac{8\pi G}{c^4}T_{\alpha\beta} \tag{1.1.1}$$

where $R_{\alpha\beta}$ is Ricci tensor which is related to the Riemann curvature tensor $R_{\alpha\beta\mu\nu}$ and R is Ricci scalar defined below.

$$R_{\alpha\beta\mu\nu} = g_{\alpha\lambda}R^{\lambda}_{\ \beta\mu\nu} = \frac{1}{2}(g_{\alpha\nu,\beta\mu} - g_{\alpha\mu,\beta\nu} + g_{\beta\mu,\alpha\nu} - g_{\beta\nu,\alpha\mu}) \tag{1.1.2}$$

$$R_{\alpha\beta} = R^{\gamma}_{\ \alpha\gamma\beta} \tag{1.1.3}$$

$$R = g^{\alpha\beta}R_{\alpha\beta} \tag{1.1.4}$$

$g_{\alpha\beta}$ represents the spacetime metric which is related to the Energy-Momentum tensor $T_{\alpha\beta}$, the source which gives rise to the curvature of spacetime. In Einstein's theory, matter and spacetime are entangled together. In words of Wheeler – " Spacetime tells matter how to move; matter tells spacetime how to curve." One key note to remember – *Einstein's theory is coordinate independent*. Thus, one is always free to choose a convenient coordinate system for calculations. We will use weak field approximation for all derivations discussed.

1.2 Gravitational Waves

As stated gravitatioanl force arise arise from the curvature of spacetime. In a special case of weak gravitational fields, the spacetime metric can be approximated as small perturbations $h_{\alpha\beta}$ ($|h_{\alpha\beta}| << 1$) to flat spacetime define by the minkowski metric $\eta_{\alpha\beta}$ (we assume signature as [-1, 1, 1, 1]).

$$g_{\alpha\beta} = \eta_{\alpha\beta} + h_{\alpha\beta} \tag{1.2.1}$$

Under the assumption of weak gravitational fields, it is valid to consider $h_{\alpha\beta}$ as a tensor in special relativity. As a result, we use the minkowski metric for raising and lowering indexes of $h_{\alpha\beta}$. The trace of h is

$$h = h^{\alpha}_{\ \alpha} = \eta^{\alpha\gamma}h_{\gamma\alpha} \tag{1.2.2}$$

We define a trace reverse tensor of $h_{\alpha\beta}$ as :

$$\bar{h}^{\alpha\beta} = h^{\alpha\beta} - \frac{1}{2}\eta^{\alpha\beta}h \tag{1.2.3}$$

The trace of the reverse tensor is $\bar{h} = -h$. From equation 1.2.3 one can rewrite h as:

$$h^{\alpha\beta} = \bar{h}^{\alpha\beta} - \frac{1}{2}\eta^{\alpha\beta}\bar{h} \tag{1.2.4}$$

Using the equations 1.1.2 and 1.2.3 to evaluate the left hand side of 1.1.1. Then to first order in $h_{\alpha\beta}$ we get:

$$G_{\alpha\beta} = -\frac{1}{2}(\bar{h}_{\alpha\beta,\mu}{}^{,\mu} + \eta_{\alpha\beta}\bar{h}_{\mu\nu}{}^{,\mu\nu} - \bar{h}_{\alpha\mu,\beta}{}^{,\mu} - \bar{h}_{\beta\mu,\alpha}{}^{,\mu}) \tag{1.2.5}$$

Under Lorentz gauge condition $\bar{h}^{\mu\nu}{}_{,\nu} = 0$, the above equation simplifies to give

$$G^{\alpha\beta} = -\frac{1}{2}\Box\bar{h}^{\alpha\beta} = \frac{8\pi G}{c^4}T^{\alpha\beta} \tag{1.2.6}$$

where $\Box$ is the d'alembertian operator. If we now consider vacuum state solutions (source is at infinity : $T^{\alpha\beta}$ = 0) of the above equation, we get travelling wave equation.

$$\Box\bar{h}^{\alpha\beta} = 0 \tag{1.2.7}$$

The solutions to the above equation can we written in form of a travelling wave in plane wave basis. The amplitude of wave is $A^{\alpha\beta}$ propagating with wave vector k_{gamma}

$$\bar{h}^{\alpha\beta} = A^{\alpha\beta}exp(ik_\gamma x^\gamma) \tag{1.2.8}$$

Using the Lorentz gauge condition on the solutions we get that $A^{\alpha\beta}$ is orthogonal to the wave propagation vector k.

$$A^{\alpha\beta}k_\beta = 0 \tag{1.2.9}$$

We exploit the gauge freedom to further constrain the amplitude. Using gauge invariant conditions we get

$$A^\alpha{}_\alpha = 0 \tag{1.2.10}$$

$$A_{\alpha\beta}U^\beta = 0 \ ; \text{ where U is the four velocity vector.} \tag{1.2.11}$$

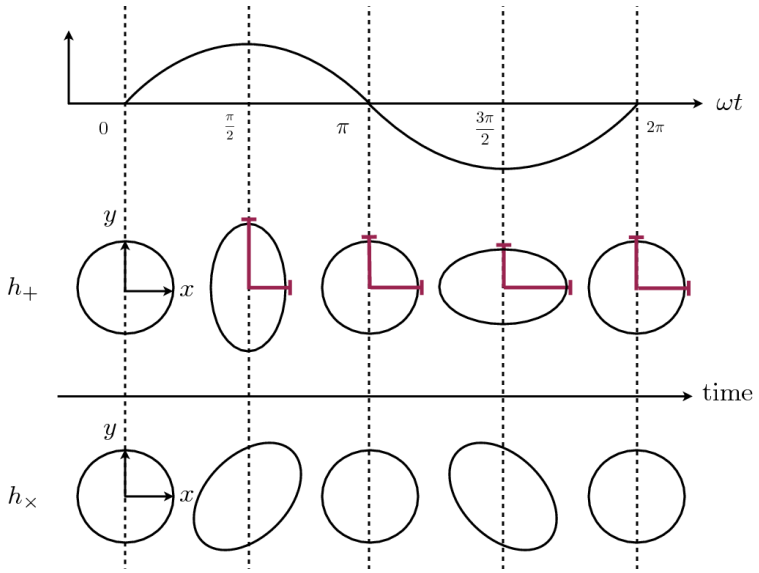

Figure 1.2: The effect of the two polarizations (h_+ and $h_\times$) of GWs on a ring of test mass particles. The figure shows how the ring is distorted over time due to the passage of purely polarized GWs.

The condition 1.2.10 requires the trace of $A^{\alpha\beta}$ to be zero. Moreover, using 1.2.10 in 1.2.3, it is straightforward to see that $h^{\alpha\beta} = \bar{h}^{\alpha\beta}$.

The conditions 1.2.9, 1.2.10 and 1.2.11 together define the *Transverse-Traceless (TT) gauge*. U is a velocity four-vector in a background minkowski spacetime, we can write it as $U^\alpha = \delta^\alpha{}_0$. Using this in 1.2.11, we get $A_{\alpha 0} = 0$ for all α. Now consider a frame such that the wave is traveling in the positive z-axis of space. In this frame 1.2.11 requires $A_{\alpha 3} = 0$ for all α.

Summarizing all the constraints above $h^{\alpha\beta}$ is symmetric and traceless, $h_{\alpha 3} = 0$ and $h_{\alpha 0} = 0$. We are left with only two independent quantities that define $h_{\alpha\beta}$. Physically, these two independent quantities are the two possible polarizations of GWs – h_+ and $h_\times$. A generalized metric satisfying the TT gauge condition can be written as:

$$h_{\alpha\beta} = \begin{bmatrix} 0 & 0 & 0 & 0 \\ 0 & h_+ & h_\times & 0 \\ 0 & h_\times & -h_+ & 0 \\ 0 & 0 & 0 & 0 \end{bmatrix} \tag{1.2.12}$$

The effect of each polarization on a ring of test mass is shown in figure 1.2. The concept of interferometry to detect GWs stems from the same picture. Kip Thorne, Ronald Drever and Rainer Weiss

put forward the idea that the differential movement of the mirrors of the Michelson interferometer could be used to detect the GWs. But the next question that arises is how much do the mirrors move due to GWs? We will address this in the next chapter.

1.3 Quadrupole approximation

Consider the equation 1.2.6. If we assume that the astrophysical source of GWs is undergoing slow motion. Also, all astrophysical sources undergo periodic motion so it is reasonable to assume that $T_{\alpha\beta}$ is undergoing sinusoidal motion with frequency Ω. With these assumptions we can write,

$$T_{\alpha\beta} = Real(S_{\alpha\beta}\, e^{-i\Omega t}) \tag{1.3.1}$$

Under the assumption of slowly moving sources, we demand that the velocity inside the source region is small ($S_{\alpha\beta} << 2\pi/\Omega$). Solving the equation 1.2.6 with these assumptions leads to the solution called as quadrupole approximation. We define the inertia tensor as the second order moment of the distribution of mass as

$$I_{jk} = \int T^{00} x_j x_k d^3x \tag{1.3.2}$$

Then the GW amplitude under quadrupole approximation is given by

$$h_{jk} = \frac{2}{r}\frac{d^2 I_{jk}}{dt^2} \tag{1.3.3}$$

In the TT gauge with the above assumptions, the independent polarizations of the GW emitted by a source at distance r is given by

$$h_{xx} = -h_{yy} = -\Omega^2(\bar{I}_{xx} - \bar{I}_{yy})e^{i\Omega r}/r \quad ; \quad h_{xy} = -2\Omega^2 \bar{I}_{xy} e^{i\Omega r}/r \tag{1.3.4}$$

where $\bar{I}_{jk}$ is called as the trace-free quadrupole moment tensor and is defined as:

$$\bar{I}_{jk} = I_{jk} - \frac{1}{3}\delta_{jk} I^{l}{}_{l} \tag{1.3.5}$$

Physical implications of the above equations are immense. Consider a system which is undergoing spherically symmetric motion, which implies that the inertia tensor is such the $I_{xx} = I_{yy} = I_{zz}$,

consequently, $\bar{I}_{xy} = 0$ and thus $h_{xx} = -h_{yy} = h_{xy} = 0$. Thus, any spherically symmetric motion will not produce GWs. Now consider a system undergoing cylindrical symmetric motion ($I_{xx} = I_{yy} \neq I_{zz}$). Using the same arguments we see this system too can not emit GWs. Using quadrupole approximation we see that any motion that is spherically or cylindrical symmetric will not emit GWs. To have a non-vanishing mass quadrupole moment is necessary for a system to emit GWs.

Given a source at a distance *r* that emits energy E in form of GWs with frequency *f* in time T. The amplitude of GWs in quadrupole approximation can be derived using the luminosity and flux equations and is approximated by,

$$A \sim \frac{1}{\pi f r}\sqrt{\frac{E}{T}} \tag{1.3.6}$$

1.4 Astrophysical Sources of Gravitational Waves

As stated, GWs can be emitted from any source which has a non-zero quadrupole moment. However, the amplitude of these waves is very small, posing a challenge in their detection for almost three decades. The astrophysical sources which emit their energy strongly in GWs are summarized below.

- Compact Binary Coalesce : black hole - black hole (BH-BH) binaries, black hole - neutron star (BH-NS) binaries, neutron star - neutron star (NS-NS) binaries, super-massive black hole binary and galaxy mergers.
- Gravitational collapse : asymmetric supernovae.
- Stochastic GW background : In our vast universe, we expect hundreds and millions of binaries inspiralling together and emitting GWs. All these together form the stochastic GW background.
- Cosmic GWs : The GWs from the Big Bang.

The figure 1.3 summarizes the frequency band of numerous possible sources of GWs [8]and detectors capable of detecting the GWs emitted by these sources. We will discuss the basic principles employed in GWs detectors in the next chapter.

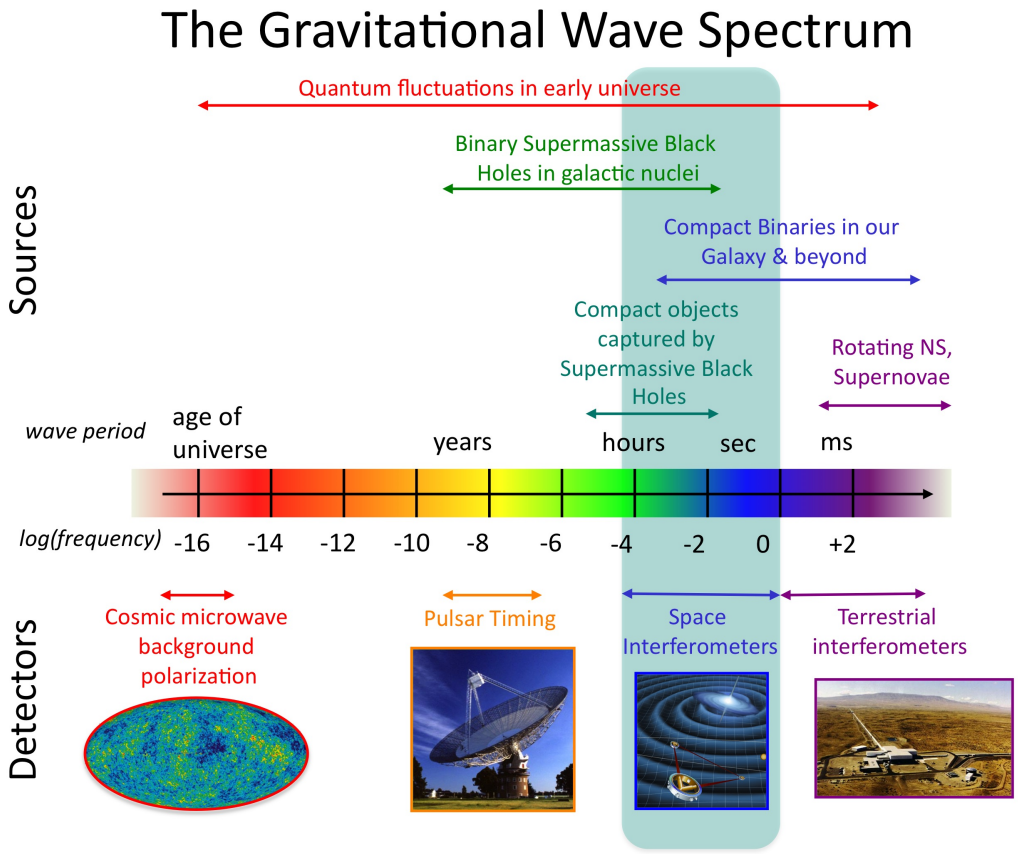

Figure 1.3: Different sources of GWs, categorized by the frequency of the emitted GWs are summarized in the figure above. The detectors which are capable of detecting the respective GW source in a given frequency bin are shown below. *Courtesy:* "Gravitational Astrophysics Laboratory". science.gsfc/nasa.gov

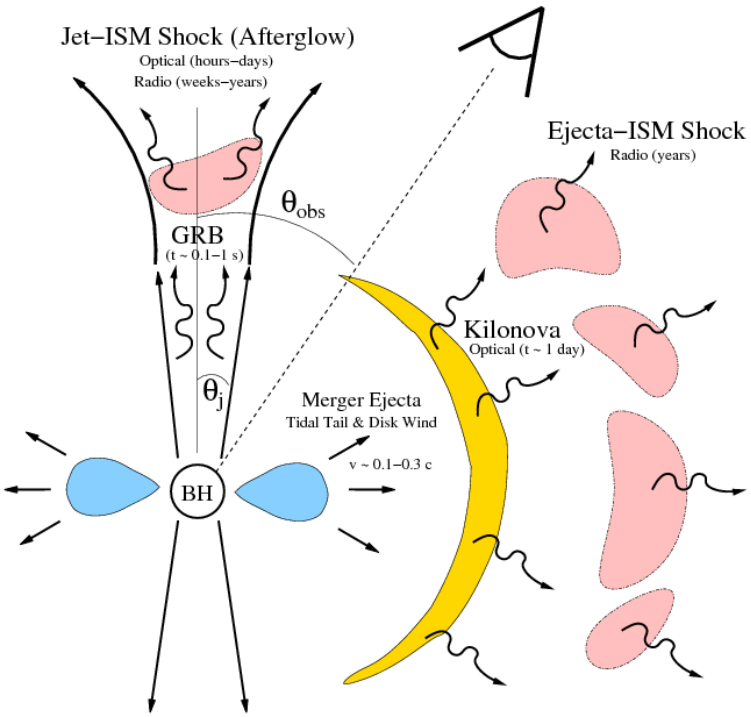

Figure 1.4: The EM counterparts of a NS-NS/NS-BH merger are summarized in the figure above. We see that the signal is distributed over the entire range of the EM spectrum – Gamma ray burst, Optical-Infrared and Radio. [1]

1.5 Electromagnetic Counterparts

Astronomers have made numerous observations of supernovae transients but we have not yet detected any GWs arising from supernovae. Mergers of NS-NS binaries are expected to emit in a range of the electromagnetic(EM) spectrum 1.4. NS-BH mergers too can emit in EM spectrum provided the ratio BH mass to NS mass is less than 5. Tidal disruption of the NS is a necessary condition for emission in EM spectrum. For higher mass ratios the neutron star is swallowed by the black hole and EM emission is not likely in such cases. Recently researchers have proposed mechanisms where, in special conditions, a BH-BH binary too can emit EM radiation. To summarize, many astrophysical processes which emit GWs are also expected to emit EM radiation. But what knowledge or insight into physics does one acquire by studying both?

The NS is a compact object whose gravitational collapse is balanced by the degeneracy pressure of the neutrons. However, if one goes inside the NS, at half-radius, the pressure will be high for unbound free quarks to exist. Quarks are known to exist in the bound state only. Thus, the NS

equation of state is fundamentally unconstrained. Many possible equation of states are proposed with different physical considerations. The equation of state effects the GW emitted. Using the combined information from GWs and the EM radiation emitted, it is possible to constrain the NS equation of state which is a big motivation to find EM counterparts to GWs.

Combining the information about the source from GWs with EM observations provides complete information about the astrophysical source (GWs: mass, spins, location. EM: distance, location, the environment around, star composition). The evolution of neutron-stars to black holes too is theoretically unconstrained. Using the combined information it is possible to study the evolution of compact objects like neutron-stars and formation of black-holes. Moreover, now astronomers have gathered strong evidence that synthesis of metals heavier than lead is not likely from supernovae events, making r-process nucleosynthesis the most likely candidate to account for the abundance of the heavier metals in the universe. This can be studied, verified or debunked by studying the EM transients of the NS-NS/ NS-BH mergers.

Unfortunately, the task of EM follow-up of a GW event is a big challenge. The GW detectors are like an antenna, multiple detectors are essential to localize the source in the sky to a few degrees. The localization can error for the first detection GW150914 [5, 6] was of the order of 600 square degrees. To scan such a large area in a limited observing time before the transients fades is one challenge. Rejecting false positives from such a large area is another challenge. The scientific community realizes these problems and aims to resolve them through collaborative efforts with projects like GROWTH (Global Relay of Observatories Watching Transients Happen), still awaiting to map a detected GW signal with its EM counterpart.

Chapter 2

Detecting Gravitational Waves

The equation 1.3.6 relates the amplitude of GW's emitted from a source at distance r from the observer, emitting an energy E in form of gravitational radiation in a time T with central frequency f. Usually, the strain of GWs is scaled to an event in Virgo cluster (distance 15 Mpc), emitting an energy of $10^{-4} M_{\odot}$ in form of gravitational radiation at a frequency of 1 kHz in 1 milli-second. Then the GW strain in equation 1.3.6 can be rewritten as.

$$h = 10^{-22}\left(\frac{E}{10^{-4}\ M_{\odot}}\right)^{1/2}\left(\frac{T}{1\ msec}\right)^{-1/2}\left(\frac{f}{1\ kHz}\right)^{-1}\left(\frac{r}{15\ Mpc}\right)^{-1} \tag{2.0.1}$$

GWs stretch and shrink the spacetime but the differential strain due to the passage of GWs is of the order of 10^{-22}. To detect changes in the length of this order was the major challenge posed in detecting GWs. Weber proposed to detect these waves with the use of resonant bar detectors. However, bar detectors are limited to narrow frequency window and failed to detect GWs. Later, Kip Thorne, Ronald Drever and Rainer Weiss proposed the use of laser interferometry to detect the GWs in a broader frequency range. With over three decades of persistent effort to detect GWs, the GWs were finally detected on 14 September, 2015 [5, 6]. In this chapter, we will discuss the basic principles employed in the detection of GWs.

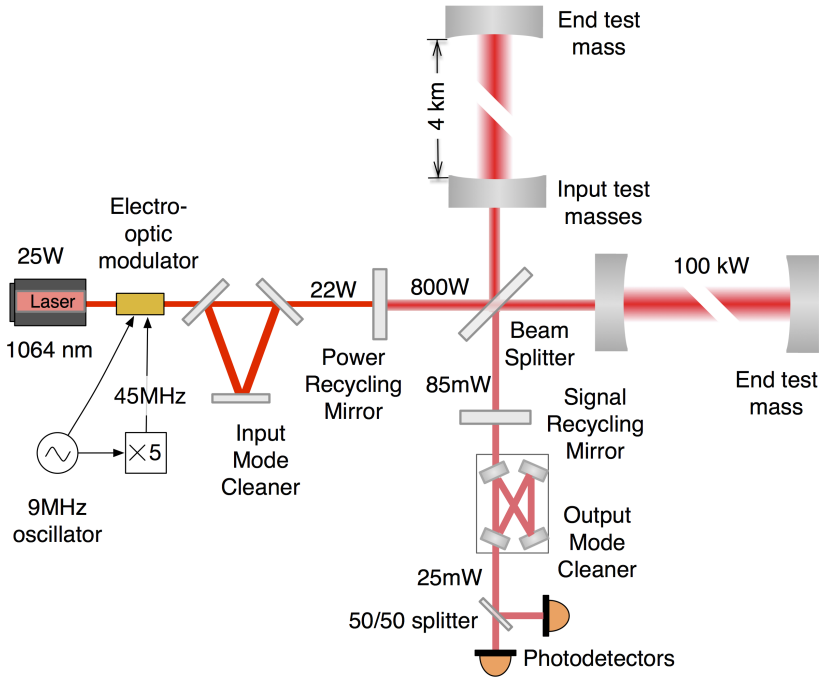

Figure 2.1: The schematic diagram of the LIGO interferometers. [2]

2.1 Laser Interferometer based Gravitational Wave Detector

Detecting GWs posed a challenge so colossal that Einstein believed the GWs will never be detected. However, decades of persistent efforts and subsequent advancements in technology made it possible to detect possible GWs. In this section, we will briefly discuss the design of the GW detectors using the concept of interferometry to detect gravitational waves. For advance understanding, one can refer to [2, 9].

Figure 1.2 depicts the distortions in spacetime caused due to GWs. As the differential motion due to GWs will cause unequal changes in the length of each arm of the Michelson interferometer. The differential change in the length of the arms can be detected by changes in the interference pattern making Michelson interferometers a natural tool to detect GWs. By using laser light as a probe to measure strain $(\Delta L/L)$ to the order of or below 10^{-22} in the arms of a Michelson interferometer it is possible to detect GWs from compact binary coalesces (CBCs). Figure 2.1 gives a schematic design of the Laser Interferometer Gravitational-Wave Observatory(LIGO). In the following subsections starting with Michelson interferometer, we will briefly describe and discuss the role of each component shown in figure 2.1.

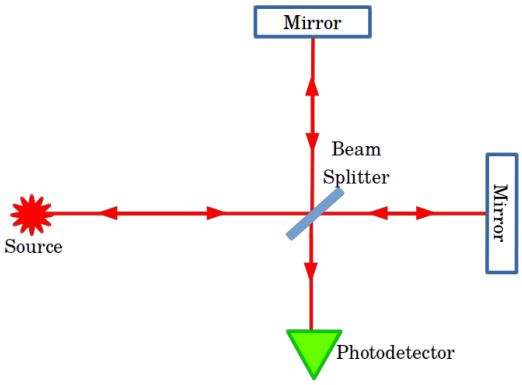

Figure 2.2: The figure shows the schematic layout of the Michelson interferometer.

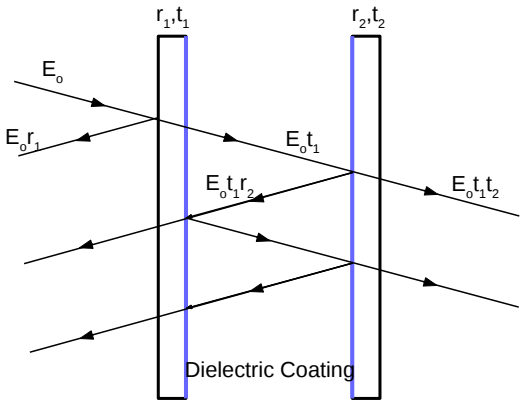

Figure 2.3: The figure depicts a Fabry-Perot cavity. The mirror reflectivity and transmittance are represented by r and t respectively. The intensity of the incoming beam is E_0.

2.1.1 Michelson Interferometer

The basic setup of Michelson interferometer is shown in figure 2.2. A laser beam is incident on the beam splitter which splits the incident beam into two orthogonal beams. Each beam traverses the arm of the interferometer. The mirrors at the end of the arms reflect them and the reflected beams from the two arms reunite at the beam splitter to give interference pattern. Any relative change in length of the arms changes the interference pattern as the optical path of each beam differs. Again there are two beams arising at the beam splitter:

- One which leaves the interferometer in the direction opposite to the beam incoming the interferometer. This beam leads to the loss of power in the arms of the interferometer. In the modified LIGO design of Michelson interferometer, the *Power Recycling Mirror* serves the purpose of minimizing the loss of power from the arms of the interferometer. The power recycling mirror is designed to have a very high coefficient of reflection.

- The second exits the interferometer in the orthogonal direction. The photodiode records the interference pattern. In the LIGO design, a *Signal Recycling Mirror* is placed in between the beam splitter and the output photodiode. It serves the same purpose as the power recycling mirror.

As stated earlier, the required sensitivity of strain$(\Delta L/L)$ to detect GWs is of the order 10^{-22}. For an arm length of 4 kms, the sensitivity required to detect changes in length is of the order 10^{-19}

m. By increasing the length of the arms the required sensitivity to detect changes in length will reduce. However, to a ground-based detector million kilometers long is impossible. To increase the optical path length in the arms multi-pass techniques are used – like a Fabry Perot cavity. However, one cannot indefinitely recycle light in a cavity due to beam alignment problems [10, 11]. Phase degradation and parametric instabilities fundamentally limit the performance of the LIGO detectors [12].

2.1.2 Electro-optic Modulator and Fabry Perot Cavity

An electro-optic phase modulator(EOM) is an optical device that can modulate the phase of a light beam, using a crystal which exhibits the Pockels effect. The Pockels effect, also called linear electro-optic effect, is the change of the refractive index in linear proportion to the electric field applied across the crystal. When an electric field is induced in a pockels crystal, the refractive index of that crystal changes. As a result, the light rays move slower in the crystal, changing the duration of time that the light takes to transverse the crystal. The phase of the light exiting the crystal is directly proportional to the time taken by the light to transverse the crystal. Thus, by varying the electric field applied across the crystal, one changes the refractive index of the crystal and thus the speed of light in the electro-optic-crystal, in this way one can regulate the duration of time the light stays inside the crystal *(t)* and thus the phase of the light coming out of the crystal can be modulated. The change in phase of the laser is given by :

$$\Delta\phi = \frac{2\pi t}{f}; \text{where f is the frequency of the laser} \tag{2.1.1}$$

In our setup, the EOM is used to modulate the phase of the laser beam and stabilizing the laser using the Pound-Drever-Hall technique [13] and a fabry-perot cavity plays a crucial role.

The Fabry Perot cavity is used to implement multi-pass in the LIGO detectors. A fabry-perot cavity consists of two parallel mirrors, light is trapped between the mirrors by the phenomenon of interference, fig. 2.3, usually coated with a dielectric material for high reflectivity. The fabry-perot cavity has a very high finesse because of the high reflectivity of the mirrors in the setup. The finesse of a cavity is defined as its free spectral range divided by the bandwidth of its resonance. The finesse is determined by the round-trip losses in the cavity. The selectivity of transmitted light can be obtained by adjusting the distance between the two mirror plates. The net transmission

through the fabry-perot cavity, disregarding the optical losses is given by:

$$T = E_o^2 \frac{t_1^2 t_2^2}{1 + r_1^2 r_2^2 - 2 r_1 r_2 cos(\omega 2L/c)} \tag{2.1.2}$$

For locking the laser, the reflected phase from the fabry perot cavity provides the signal. When the laser passes through the EOM crystal, phase modulation side-bands are introduced onto the monochromatic laser light. At resonance, the reflection coefficient of the fabry-perot cavity ideally falls to zero, and the monochromatic laser and the side-bands introduced by the EOM, are all reflected with the same phase.

The higher the finesse, the sharper the resonance and steeper the change in phase with respect to the change in length of the cavity. This property of the fabry-perot cavity enables us to measure the change in cavity length accurately once the laser is locked. The change in length of cavity signifies the drift from resonance and this is used to design the servo for locking the cavity.

Once the LASER is locked, we use Pound-Drever-Hall Technique to measure the small changes in the length of the cavity caused due to thermal noise and with a help of a feedback servo, compensate for the changes in the length accordingly. For a brief understanding, one can refer to a nice review article on the technique [13].

2.2 Sources of Noise

GWs are detected by interferometry by which we measure the arm length over time. However, any changes in the length of the interferometer arm can be attributed to distortions caused by GWs, only if the length of the cavity is stable upto an order of a few fermi-meters. However, there are numerous fluctuations which are cause distorsions of this order by contributing to instrumental noise. These factors which influence the length measurement can be broadly sub-divided into two categories – one physically fundamental in nature while the other which are caused due to the environmantal factors.

- Fundamental constraints

    1. Displacement Noise – Heisenberg uncertainty principle fundamentally limits the accuracy with which the position of the mirror. Measurements in mirror motions are

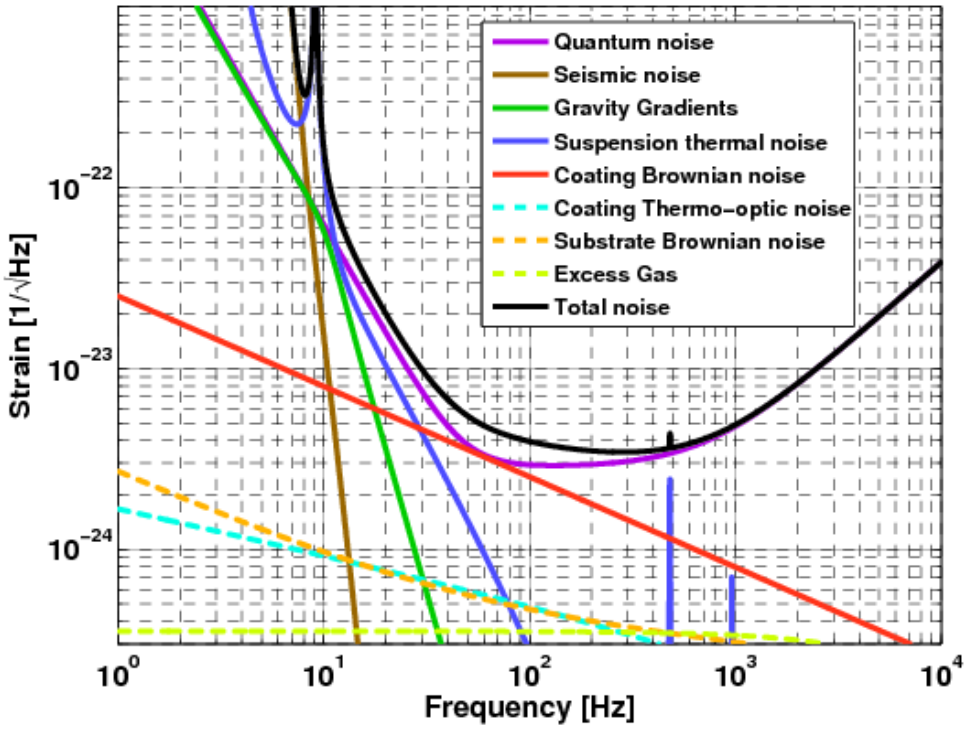

Figure 2.4: The figure summarizes the different noise sources which limit the advanced-LIGO detector sensitivity over the range of frequency. [3]

limited in accuracy by the relation $\Delta x \cdot \Delta p \geq \hbar$. If the data is collected at a sampling frequency *f*, the time interval between measurement is τ. Then for a mirror of mass M, $\Delta p \sim M\Delta x/\tau$. The sensitivity to measure gravitational strain $(\Delta x/L)$, where L is the optical path length in an interferometer, is limited by the uncertainty relation to $\sqrt{\hbar\tau/ML^2}$. Thus, the quantum limit can be reduced by increasing the mass of the mirror and the optical path of the photon. Increasing the sampling frequency also improved the sensitivity.

2. Shot Noise – Due to the particle nature of light, we have a discrete number of photons in the laser beam. The photodetector detects the photon s similar to a counting process, which is poissonian in nature. Thus, for any detection of N photons, there is an inherent error of $\sqrt{N}$ (shot noise).

3. Radiation Pressure Noise – The flux of photons carry a momentum which causes the test mirrors to move.

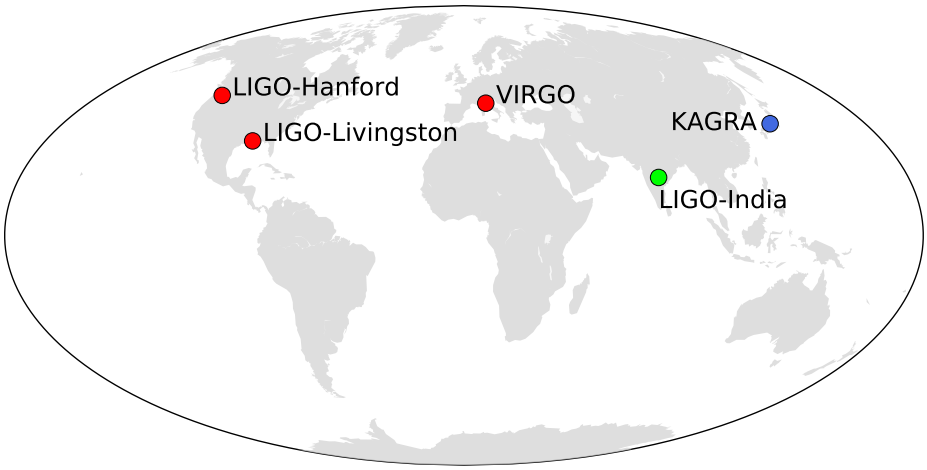

Figure 2.5: Location of the GW detectors across the globe.

- Instrumental and Environmental sources

    1. Seismic Noise – The seismic motion from the earth can cause mirror displacements in much greater order of magnitude than displacements due to the passage of GWs. To avoid this, mirrors are suspended with anti-spring blades which compensate against the ground motion keeping the mirror intact. The residual motion of the mirrors due to the movement of heavy masses nearby, earth, etc lead to seismic noise. Better suspension systems are aimed to reduce seismic noise contributions.

    2. Suspension Thermal Noise – The thermal fluctuations in the fiber which hangs the mirror.

    3. Coating Thermal Noise – The mirrors all have dielectric coatings over them. The brownian motion of atoms and molecules over the mirror gives rise to irregular beam scattering. To reduce the coating thermal noise, a straight forward answer is to find materials with better mechanical properties. Other more sophisticated measures include increasing the beam size, reducing coating temperature, using specific modes of the laser [3].

Other noise sources include gravity gradient noise, residual gas noise, etc. The contribution of each noise source in the advanced LIGO design is shown in figure 2.4 [3].

The currently working, under construction and proposed GWs detectors across the globe are shown in figure 2.5

1. LIGO Hanford and LIGO Livingston (USA): Arm length of 4 kms.
2. VIRGO (Italy): Arm length of 3 Kms, currently under upgrade but will soon start observing.
3. GEO (Germany): Arm length of 600 m.
4. KAGRA (Japan): A cryogenically cooled detector with an arm length of 3 Kms under construction in Japan.
5. LIGO-India (approved): Arm length of 4 Kms.

2.3 Gravitational Wave Data Analysis

The primary sources that can be detected by LIGO are compact binary coalescence (CBCs). Einstein's theory of general relativity predicts for any stellar binaries emit GWs, their orbit shrinks over time and the stellar objects in binaries ultimately merge. The GWs emitted from NS-NS binaries, NS-BH binaries and BH-BH binaries (upto few hundreds $M_{\odot}$), can be detected by the ground-wave detectors 1.3. However, the signal can be buried in noisy data. Extracting the signal correctly and the correct signal is another challenge. During the process of analyzing the data, we have to be cautious to ensure and check that instrumental glitches which can mimic the signal are vetoed and only the signal from the astrophysical sources is considered. That is we have to reduce the false alarm ratio. In this section, we will start with discussing the source parameters which determine the emitted GW waveform. Then, we will subsequently build on how the data accumulated is analyzed.

2.3.1 Waveform and CBC search space

To get the solutions to waveforms arising from CBCs in Einstein's general theory of relativity one has to solve the metric equation with source terms. The problem is extremely complicated it involves partial differential equations that are coupled and nonlinear in nature. In the few simpler systems the Einstein's equations have been analytically solved – Schwarzschild solution to

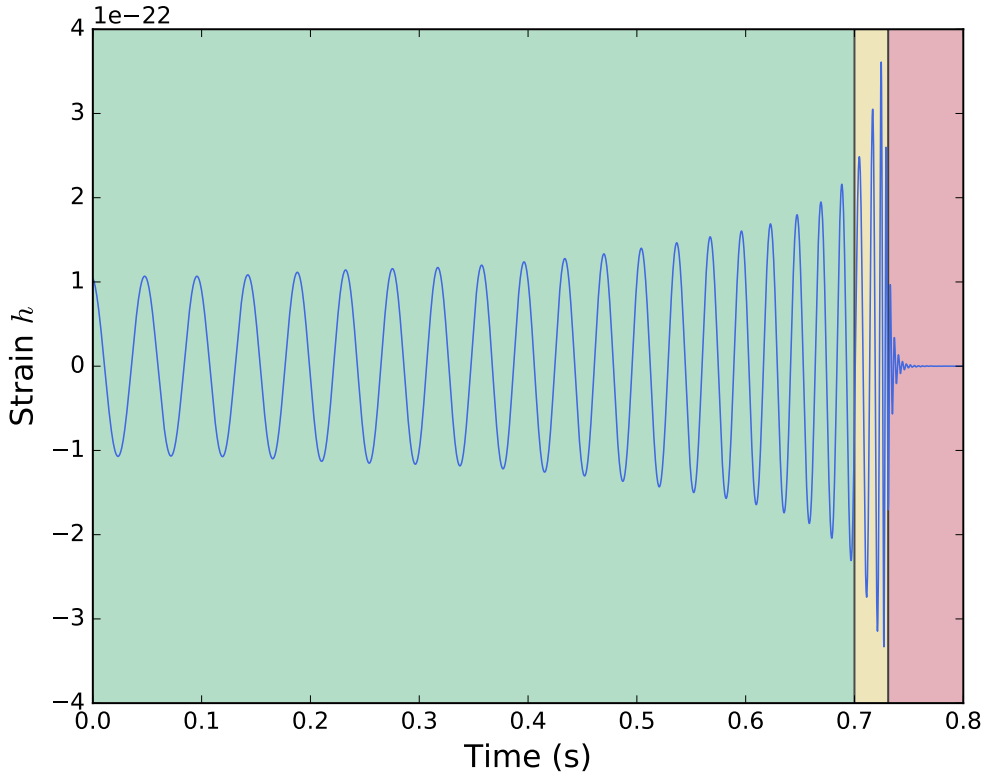

Figure 2.6: The figure shows a typical GW waveform due to compact binary coalesce. The above waveform arises from to the coalesce of a 35-30 $M_{\odot}$. The green, yellow and pink regions respectively represent the inspiral, merger and ringdown phases of the evolution of the binary system.

non-spinning spherically symmetric single stellar object and Kerr solutions for spinning objects. However, to date no analytic solutions exist for a binary system and the gravitational radiation they emit. The next best approach to overcome the problem with the use of computers and obtain numerical solutions to the Einstein's equation. The field in GW physics which tries to find numerical solutions to Einstein's equation is called *Numerical Relativity*. However, solving Einstein's equation numerically is both complicated and computationally expensive. To use numerical relativity to generate a single GW waveforms from CBCs can take a few months. But, to extract the GW signal buried in noise, one typically requires millions of GW waveforms (Why? We will discuss soon). These GW waveforms are generated such that they sample the entire range of astrophysical sources that the ground-based GW detectors can detect. The use of numerical relativity to generate the GW waveforms for a few millions of astrophysical sources is almost impossible. To solve this problem one uses approximants which can generate GW waveforms faster.

The Post-Newtonian(PN) theory [14] is widely used to generate approximant GWs waveform. The theory approximates the Einstein's equation as a Taylor series expansion in powers of $\sqrt{v/c}$. The terms in the Taylor series expansion can be regarded as perturbations or deviations from Newton's classical theory of gravity, thus the name PN theory. The waveforms generated using PN theory have been tested and found consistent with the ones from numerical relativity in the inspiral part of the waveform 2.6 (upto ISCO). The ringdown part of the waveform is computed using the black hole perturbation theory. The merger phase is the most complicated and one replies on NR simulations for this part. Lastly, the three fragments Inspiral, Merger and Ringdown (IMR) are stitched together to get an approximant GW waveform called IMR waveform.

The parameters effecting the GW waveform from a CBC source are summarized below.

1. m_1 and m_2 : Masses of the two stellar objects orbiting each other to form a compact binary.
2. $\boldsymbol{S_1}$ and $\boldsymbol{S_2}$: The spin vectors of the two stellar objects.
3. D : Distance of the binary from Earth.
4. ι : Inclination of the orbital plane of the binary with respect to the line of sight.
5. θ, ϕ : The declination and the right-ascension of the binary.
6. Ψ : The polarization of the GW emitted.
7. ϕ_o : Reference phase for the signal.
8. t_o : Reference time for the signal.

The mass and spins parameters are intrinsic parameters of a CBC while the remaining parameters are extrinsic. Any search for a GW signal in the LIGO data stream searches for these parameters. As stated earlier to extract the signal from the noise required millions of templates. Typically, many searches consider the intrinsic spin of compact objects in binaries to be aligned or anti-aligned with the orbital angular momentum $\mathbf{L}$. Allowing for general three-dimensional spin leads to precession of the spin with respect to the orbital angular momentum. The GW waveform is also modulated. However, to save computational cost the spin-precessing binaries are ignored in certain GW searches. We too in our subsequent analysis, discussed in chapter 4 consider cases where the intrinsic spin is either aligned or anti-aligned with the orbital angular momentum $\mathbf{L}$.

2.3.2 Notations

The data recorded by the LIGO detectors is a time-series of mirror positions (t_i, x_i). We represent the recorded strain as a function of time by $s(t)$. This strain is comprised of noise $n(t)$ but if there is an astrophysical event leading to the emission of GWs which are strong enough to produce detectable strain in the detector. Then, the detector also records he strain $h(t)$ due to the GW signal. Thus, for the time instants where the data has signal embedded in noise we have strains $s(t)$ as:

$$s(t) = n(t) + h(t) \tag{2.3.1}$$

When searching for a GW signal in a segment of data, we essentially seek to distinguish between the two cases

1. Null Hypothesis $\mathcal{H}_0$: s(t) = n(t). The data strain has no GW signal.

2. Test Hypothesis $\mathcal{H}_1$: s(t) = n(t) + h(t). The data strain has signal from an astrophysical source embedded along with noise.

In mathematics, one defines an *odds ratio*, as the ratio of the probability that the test hypothesis is true to the probability of null hypothesis bring true. In our formulation, where we aim to detect GWs embedded in noise, the odds ratio can be expressed as $\mathcal{O}(\mathcal{H}_1|s)$ = P($\mathcal{H}_1$|s) / P($\mathcal{H}_0|s$).

We will be using fourier transforms in subsequent discussions with this consistent definition. We define fourier transform of a time series $x(t)$ as:

$$\tilde{x}(f) = \int_{-\infty}^{\infty} x(t)\, e^{-2\pi i f t} dt \tag{2.3.2}$$

The inverse fourier transform is defined as:

$$x(t) = \int_{-\infty}^{\infty} \tilde{x}(f)\, e^{2\pi i f t} df \tag{2.3.3}$$

We know that instrumental noises are random in nature. However, we can determine statistical properties of a random process, which can, in turn, be used to understand instrumental noises and develop data-analysis techniques. The random processes can be divided into sub-categories based on their statistical properties – stationary and independent. A random process is deemed stationary if the statistical properties are time independent. Any observations of statistical quantities or moments dont change over time. Thus for a stationary random processes, the mean (or higher

moments) is equal to the average of time-series $x(t)$ over a long time T.

$$\langle x \rangle = \lim_{T\to\infty} \frac{1}{T} \int_{-T/2}^{T/2} x(t)dt \tag{2.3.4}$$

For a more detailed understanding of the concepts employed in GW data analysis one can refer to [15].

2.3.3 Power Spectral Density

The power spectral density (PSD) or power spectrum is the distribution of energy as a function of frequency. It represents at any given frequency what is the energy carried by a wave. In GW detectors the PSD of noise quantifies the sensitivity of the detector.

If we consider a signal $x(t)$ which is a stationary random process in nature. The energy carried by the signal in time T can be calculated by integrating $x^2(t)$ over time T. Power is the rate of change of energy. Thus, dividing the energy transmitted in time T by the time interval T we get the power transmitted by the signal. We have assumed that the signal is stationary, so the time average of $x^2(t)$ is equal to the expectation value of $\langle x^2 \rangle$. Implying

$$\langle x^2 \rangle = \lim_{T\to\infty} \frac{1}{T} \int_{-T/2}^{T/2} x^2(t)dt \tag{2.3.5}$$

Using fourier transform of $x(t)$ and Parseval's theorem the above equation leads to the defining equation of PSD of a stationary random process.

$$\langle x^2 \rangle = \int_0^\infty S_x(f)df \tag{2.3.6}$$

$$S_x(f) := \lim_{T\to\infty} \frac{2}{T} \left| \int_{-T/2}^{T/2} x(t)\, e^{-2\pi i f t} dt \right|^2 \tag{2.3.7}$$

Integrating the 2.3.7 with $t = t^{'} + \tau$ we get the PSD for a stationary random process related to the signal auto-correlation function R_x as:

$$S_x(f) = 2\int_{-\infty}^{\infty} R_x(\tau)\, e^{-2\pi i f \tau} d\tau \quad \text{where} \quad R_x(\tau) = \langle x(t)x(t+\tau) \rangle \tag{2.3.8}$$

The above results hold true for a stationary random process without any assumption on the distri-

bution function of the random variable. If we consider gaussian noise (the distribution function is gaussian) then we can define the *noise-weighted inner product* of two time-series as:

$$\langle a|b\rangle := 4\ Re\ \int_0^\infty \frac{\tilde{a}(f)\tilde{b}^*(f)}{S(f)}df \tag{2.3.9}$$

$$= \int_{-\infty}^{\infty} \frac{\tilde{a}(f)\tilde{b}^*(f) + \tilde{a}^*(f)\tilde{b}(f)}{S(|f|)}df \tag{2.3.10}$$

2.3.4 Bayesian Inference

Bayesian Inference is an important recipe used in statistical inference which uses Bayes's theorem to improve the probability of a hypothesis as more data (evidence) is accumulated. Consider a hypothesis *H* and an experimental observation *O*. Bayes's theorem states the probability of the hypothesis H being true given we make an observation O is $P(H|O)$ (posterior probability) given by:

$$P(H|O) = \frac{P(H)\ P(O|H)}{P(O)} \tag{2.3.11}$$

$P(H)$ (prior probability) is the probability of the hypothesis being true regardless of the observations made. $P(O)$ (marginalized likelihood) is a normalizing factor, constant across all the hypothesis. $P(O|H)$ (likelihood) is the probability of making a positive observation given that the hypothesis H is true. In words, Bayes's theorem makes the statement that the posterior probability is proportional to prior probability and likelihood. Using this proportionality it is easy to show $P(O) = P(H)P(O|H) + P(\widetilde{H})P(O|\widetilde{H})$, which when inserted into equation 2.3.11 yields

$$P(H|O) = \frac{P(H)\ P(O|H)}{P(H)P(O|H) + P(\widetilde{H})P(O|\widetilde{H})} \tag{2.3.12}$$

$$= \frac{\lambda(H|O)}{\lambda(H|O) + P(\widetilde{H})/P(H)} \tag{2.3.13}$$

where $P(\widetilde{H})$ represents the probability that the hypothesis H is false, $P(\widetilde{H}) = 1 - P(H)$ and we define *likelihood ratio* as

$$\lambda(H|O) := \frac{P(O|H)}{P(O|\widetilde{H})} \tag{2.3.14}$$

2.3.5 Matched Filter and Likelihood

In the detection of GW from noisy data, as stated earlier, is essential to differentiate between the two hypothesis defined in section §2.3.2. The two hypothesis can be reframed as one which has no GW signal present – the null hypothesis $\mathcal{H}_0$. The other $\mathcal{H}_1$ with the GW signal embedded in noise. We can now define the likelihood ratio that given a data stream what are the chances it contains a GW signal to the chances of the data being only detector noise. Using equation 2.3.14, the likelihood ratio for this case becomes:

$$\lambda(\mathcal{H}_1|s) = \frac{p(s|\mathcal{H}_1)}{p(s|\mathcal{H}_0)} \tag{2.3.15}$$

Assuming stationary gaussian noise, we have $p(s|\mathcal{H}_0) \propto e^{-\langle s|s\rangle/2}$. If the hypothesis $\mathcal{H}_1$ is true, then, $n(t) = s(t) - h(t)$. In this case, we can write $p(s|\mathcal{H}_1) \propto e^{-\langle s-h|s-h\rangle/2}$. Substituting these expressions in equation 2.3.15, we can write the likelihood ratio as

$$\lambda(\mathcal{H}_1|s) = \frac{e^{-\langle s-h|s-h\rangle/2}}{e^{-\langle s|s\rangle/2}} \tag{2.3.16}$$

When trying to detect GW with PSO algorithm we will use the likelihood function in equation 2.3.16 as the fitness function to be optimized. On simplifying the above equation one step further we get

$$\lambda(\mathcal{H}_1|s) = e^{\langle s|h\rangle} e^{-\langle h|h\rangle/2} \tag{2.3.17}$$

We see an interesting result that the likelihood function is a monotonically increasing function of $\langle s|h\rangle$. Now, if one needs to define detection thresholds on the likelihood function, we can translate these thresholds to thresholds on $\langle s|h\rangle$, making it an optimal detection statistics. The function $\langle s|h\rangle$ is called the matched filter which we had defined in equation 2.3.9. We will also use the matched filter as a fitness function to be optimized using PSO.

Chapter 3

Particle Swarm Optimization

The particle swarm optimization (PSO) algorithm was developed by Kennedy and Eberhart [16]. The algorithm was inspired by the social behaviour of a swarm of birds or a school of fishes. Although the aim was to mimic and understand the social behaviour of animals, it was observed that swarms converged to optimal solutions of the given function in the parameter space. We know from Darwinian theory that through evolution species acquire traits which enhance their chances of survival. Being social by being symbiotic is one of the traits which helps to improve the survival chances. Thus, one can say for some birds, fishes, ants etc. that evolution gave rise to their social behaviour. Modelling social behaviours with PSO indirectly models this evolution mechanism. For this reason, many compare PSO algorithm to evolutionary algorithms like the genetic algorithm.

In this chapter, we will first describe the PSO algorithm §3.1. Then we will discuss the simplest multi-swarm extension to the standard PSO technique §3.2. In sections §3.3 we will describe the variant developed during the course of the project followed by its applications and advantages in section §3.4 and §3.5.

3.1 Particle Swarm Algorithm

Consider a large flock of birds which have collaborated their efforts to search for the best corn field in a given area. As we consider the swarm being social, we make a simple assumption that all birds (particles) can interact and communicate with all the other members of the swarm, irrespective of

the distance between them. The aim of the swarm is to cooperate and find the best corn field (global best) in the region of survey (parameter space) and ultimately all the particles in the swarm converge to this location.

To start off with, we assume that all the birds are randomly distributed in the parameter space. Over time we allow the birds to explore the parameter space. The velocity of any individual bird (particle) in the swarm is influenced by three factors

1. *Inertial weight* : At any given instance of time, the particles in the swarm have with some velocity. Due to their inertial weight, the particles will continue to move in the same direction. The velocity at any instant of time depends on the velocity before. In PSO 3.1.2, we define a parameter ω to determines the strength of the inertial weight.

2. *Personal Best (pBest)* : During the exploration, each particle keeps track of the best location it came across (personal best). At any instant of time, each particle has an instinct to stop the search and get back to its personal best location. We are free to choose the attraction potential, in standard PSO, the attractor potential is harmonic in nature. The parameter γ_p determines the strength of the attractor potential. The urge at any instant of time to get back to the personal best location is modelled by a stochastic parameter r_p.

3. *Global Best (gBest)* : As all the particles in the swarm can communicate with each other, they are collectively aware of the best location discovered by the swarm (global best). Similar to personal best, each particle has an urge to give up the search and get to the global best location. The instinct is determined by the stochastic parameter r_g while γ_g defines the strength of the global best attractor.

A major advantage of the PSO technique is that it does not use the gradient of the function to be optimized. As a result, PSO can be used to find optimal solutions of a non-differentiable equation. The time is discretized in steps of one. With the knowledge of velocity at time t, we can combine the above factors to calculate the velocity at a later time (t+1), see figure 3.1 for a diagrammatic representation of the velocity equation. The velocity at any time t is used to get the updated position. The equations governing the position and velocity are

$$x_{i,d}(t+1) = x_{i,d}(t) + v_{i,d}(t) \tag{3.1.1}$$

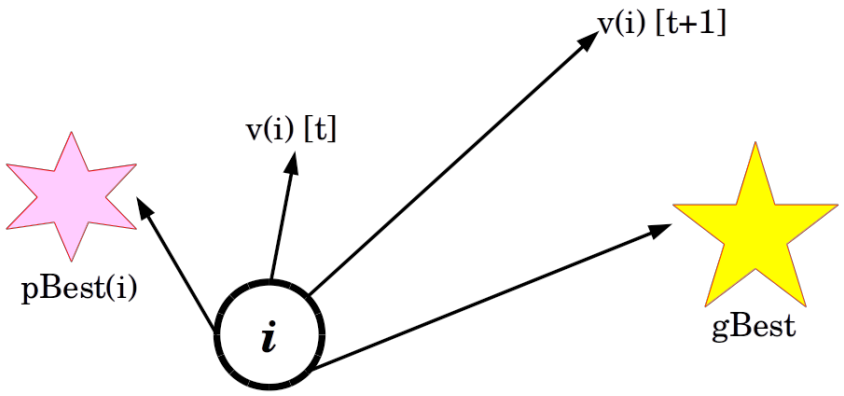

Figure 3.1: At any instant of time, the factors which influence the velocity of a particle in PSO.

$$v_{i,d}(t+1) = \omega \cdot v_{i,d}(t) + \gamma_p \cdot r_p \cdot \Big(p_{i,d}(t) - x_{i,d}(t)\Big) + \gamma_g \cdot r_g \cdot \Big(g_d(t) - x_{i,d}(t)\Big) \tag{3.1.2}$$

In the above equations, the subscript i represents the i^{th} in the swarm. The subscript d represents the dimension and t marks the successive iterations.

The PSO algorithm to optimize over a function f, called the fitness function using PSO in a bound region $\mathcal{S}$. We first initialize the swarm as

1. Distribute N particles randomly in the parameter space $\mathcal{S}$. The position vector of i^{th} particle is denoted by x_i.

2. Initially, each particle's personal best location is identical to its position vector at time t = 0.

3. To initialize the global best, compute the function f at each location $x_i[t = 0]$. By definition global best gBest = minimum$\Big($f(x_i)$\Big)$.

4. To each particle assign a velocity v at time t = 0.

Following the initialization the swarm is iteratively evolved until a termination condition is satisfied (say for M steps). Each looped iteration involves the following

1. Update the position : x_i(t+1) = x_i(t) + v_i(t).

2. Updating the personal best of each particle : if $f(x_i(\text{t+1})) < f(pBest_i) \rightarrow pBest_i = x_i(\text{t+1})$.

3. Updating the global best of the swarm : if $pBest_i <$ gBest $\rightarrow$ gBest = $pBest_i$.

4. Calculate the updated velocity using equation 3.1.2.

3.2 Multi-Swarm Optimization

One standard extension to the standard PSO technique is to use multiple sub-swarms, independent of each other, to explore the parameter space of the function which we want to optimize. The use of multiple swarms is more efficient than standard single swarm when the parameter space has multiple local optima. The efficiency of PSO does not scale linearly with the increasing number of particles. The use of multiple swarms instead proves beneficial. As each sub-swarm independently searches the parameter space, the chances of any one to get to the global optimal location is improved.

We propose a variant of the PSO which uses multiple sub-swarms to search the parameter space. To compare the efficiency of our variant we will use the standard PSO and its multi-swarm extension (Mult-PSO).

3.3 Hostile Particle Swarm

Many species of animals maintain territories and have a hostile attitude towards any intruders. We translate this idea into the swarms and see how do the search capabilities of the swarms' change. We see many interesting results and applications of this variant which we will discuss in the next section.

Given a function f whose optimal solutions are of our interest in a region of space $\mathcal{S}$ (parameter space). Instead of allowing the multiple sub-swarms independently searching the parameter space, we instead attribute hostile nature amongst the sub-swarms. To incorporate this hostile nature we use a repulsion potential. There are two ways to implement the repulsion. One where a particle of sub-swarm A is repelled from the pBest and gBest of all particles of sub-swarm B, C.... However, this adds greatly to the computational cost. The second way is to repel all particles of sub-swarm A from only the gBest location of all the other sub-swarms B, C.... See figure 3.2

In our study, we choose to incorporate repulsion in a way that all particles in any given sub-

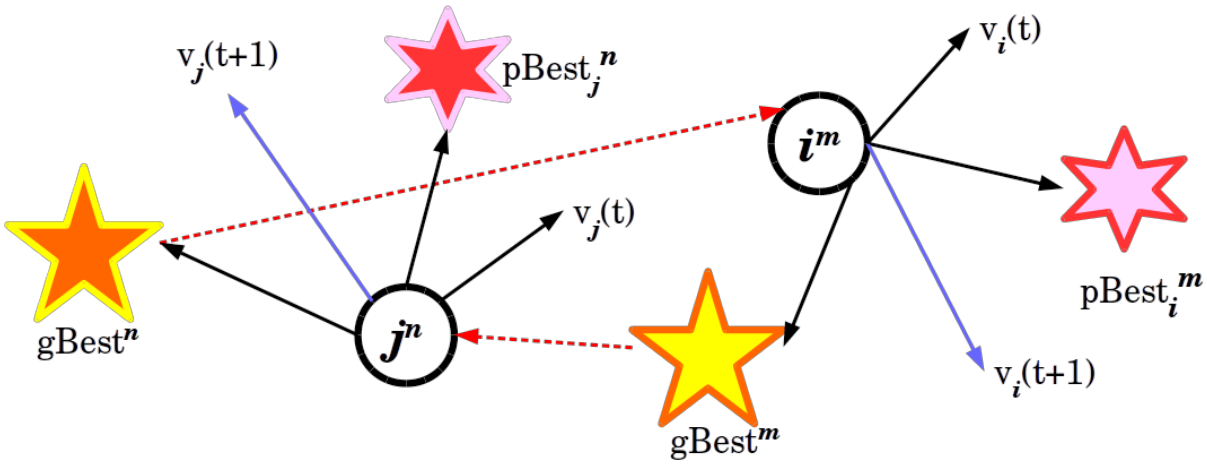

Figure 3.2: A schematic diagram illustrating the hostile swarm variant of PSO.

swarm, at any instant of time, are repelled from the gBest locations discovered by the other sub-swarms. We introduce a parameter γ_r to define the strength of repulsion potential. When any particle is repelled from the other swarm, the fight or flight response at any time is modelled by a stochastic parameter r_r. Incorporating these factors, the velocity equation 3.1.2 for a sub-swarm m is modified to:

$$v_{i,d}^m(t+1) = \omega \cdot v_{i,d}^m(t) + \gamma_p \cdot r_p \cdot \left(p_{i,d}^m(t) - x_{i,d}^m(t)\right) + \gamma_g \cdot r_g \cdot \left(g_d^m(t) - x_{i,d}^m(t)\right) - \sum_{\substack{n \\ n \neq m}} \gamma_r \cdot r_r \cdot \mathcal{F}\left(g_d^n(t) - x_{i,d}^m(t)\right) \tag{3.3.1}$$

where $\mathcal{F}$ represents a repulsion potential. We use an electrostatic or a linear repulsion potential in our study.

It is straightforward to see that there is a great possibility to drive the convergence unstable in this algorithm. In cases where two or more sub-swarms end up exploring the same gBest location, then the repulsion drives the system unstable hindering the convergence of swarm. This can be beneficial in cases when we are trying to find optimal solutions for rapidly changing function. This may be a problem in some cases but can be addressed with a slight modification which we will discuss subsequently. One can implement a hostile swarm search in multiple ways, we will compare the versions on a test function f comprising of three non-degerate gaussian peaks. The ways to simulate and search with hostile sub-swarms are,

1. Simultaneous $(Simul)$ or Relay $(Relay)$ Search : In hostile swarm variant, each sub-swarm cooperates with members of the same swarm but is repelled from the gBest location of all other sub-swarms. Thus, given m sub-swarms with $(n_1, n_2, ..., n_m)$ particles. We can either evolve all the sub-swarms together, each sub-swarm searching the parameter space simultaneously. Otherwise, a second method in which the sub-swarms have a relayed search. That is, we allow the sub-swarm 1 with n_1 particles to explore, followed by the sub-swarm 2 with n_2 particles but this time each particle of this sub-swarm is repelled from particles of sub-swarm 1. Following sub-swarm 3 will be evolved to search being repelled from both sub-swarms 1 and 2 and so on.

2. Distance constrainted Search : As stated earlier, if multiple sub-swarms end up discovering the same gBest location, it affects the convergence of the sub-swarms. One way to overcome this problem is to allow a small distance or a box around the gBest of each sub-swarm, where the gBest of any other sub-swarm is not possible. We will refer to this distance as D_c for future references. However, there is a big problem if the process is applied naively. Swarms can converge to fake or *unrealistic peaks* not present in the system. This scenario is explained using the figure 3.3. Moreover, even in cases where the sub-swarms converge to a different optimal solution in parameter space, the presence of the repulsion potential influences the convergence 3.4. Solution to both the problems, fake peaks and convergence can be solved by ending the simulation with few iterations (5 to 10) of standard PSO. *Caution: When we set the last standard PSO run – re-initialize the velocity of the particles in the sub-swarms!* By doing so, particles trapped in fictitious peaks converge to the nearby global or local optimal solution. The trend observed in figure 3.4 also disappears as the repulsion potential is removed.

To summarize the various possibilities to implement a hostile swarms search are:

1. Simultaneous search without any distance constraint.

2. Relayed search without any distance constraint.

3. Simultaneous search with a distance constraint D_c.

4. Relayed search with a distance constraint D_c.

We will present the results for each of the search method stated above in all our simulations in section §3.4.3.

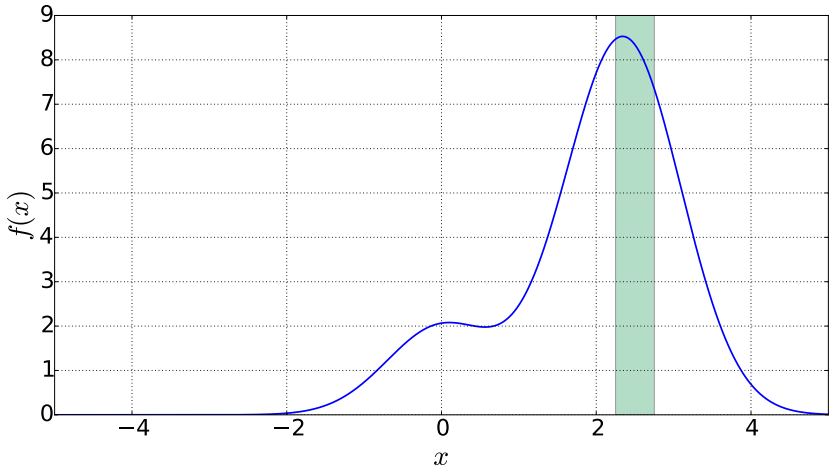

Figure 3.3: The distance constraint around the global best will carve out the area shaded in green from the parameter space. In doing so, the location where line cuts the curve becomes a fictitious peak arising due to the constraint.

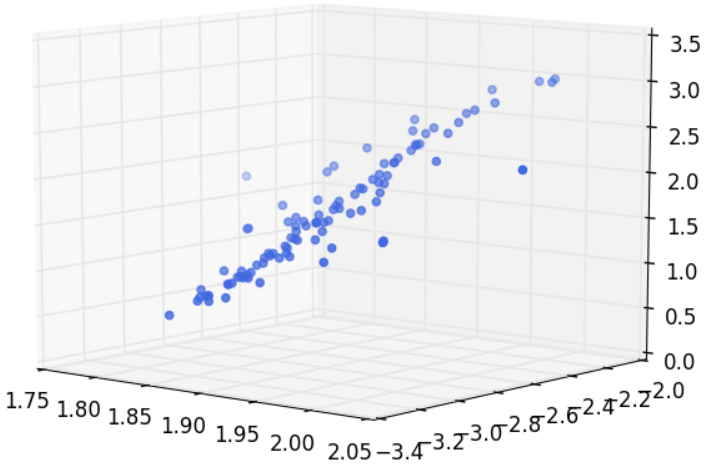

Figure 3.4: The plot shows the particles in a sub-swarm fail to converge due to the effect of the repulsion potential. The particles tend to drift away from the optimal location due to the repulsion force from the other sub-swarm.

3.4 Applications

We will test our variant with a fitness function comprising of three non-degenerate gaussian peaks in N dimension, where we can vary N = 1, 2, 3, ... and so on. We will measure the performance of our algorithm against the standard PSO. In our analysis, we first determine the number of particles required to find the global best in the case of standard PSO algorithm. Next, we will use the same number of particles to build hostile sub-swarms.

We will characterize hostile swarms algorithm by discussing the variation in performance of hostile swarms algorithm with the ratio of split in the subsection §3.4.1. However, a more basic question that arises is how does one quantify performance. As our interest is to ensure the sub-swarms explore different regions and thus, different regions of the parameter space. We measure performance by checking out of 1000 trials how many lead to different peaks in the parameter space. One also has the liberty to choose the repulsion potential between the sub-swarms. We will compare the performance between the hostile swarms with electrostatic repulsion potential and linear repulsion potential in subsection §3.4.2. Next, we will compare the performance between the simultaneous and relay search methods – with or without the distance constraint in §3.4.3. Lastly, we will discuss the advantages of this method by showing the improved chance of detecting the global best peak §3.4.4 and detecting degenerate peaks simultaneously.

3.4.1 Varying Number of Particles

As stated earlier, our *test fitness function* f comprises of three gaussian peaks of different peak strengths. *The peak values of the three gaussians in our test functions are six, three and two respectively.* As we try to find a global solution in higher dimensions using the standard PSO, we increase the number of particles. The number of particles used in the standard PSO technique in N dimension is referred to as Np_{pso}. The number of particles used to survey the parameter space in PSO with different dimension is summarized in table 3.1.

When we use hostile swarms, we split the particles Np_{pso} into two hostile swarms. This division of particles can be asymmetric. The sub-swarm with the higher number of particles is called as primary sub-swarm, while the other is referred to as secondary sub-swarm. We vary the ratio of particles in the primary to secondary sub-swarm as 2:1, 5:3, 4:3 and 1:1. That is, the secondary swarm has 0.5, 0.6, 0.75 and 1 times the particles in the primary swarm. We determine the number

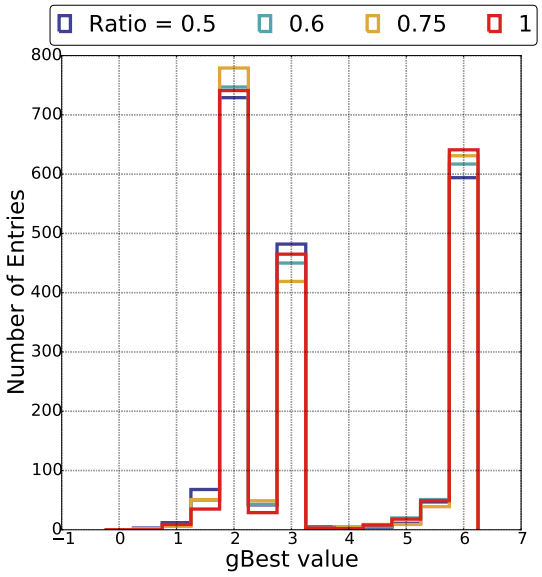

Relayed search with $D_c = 0.5$.

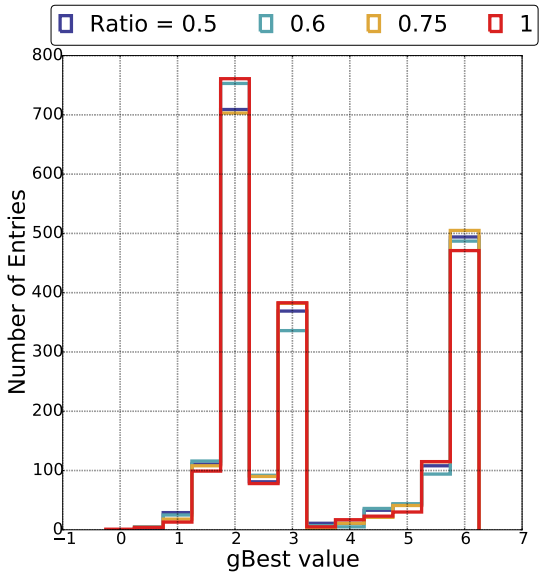

Relayed search without any distance constraint.

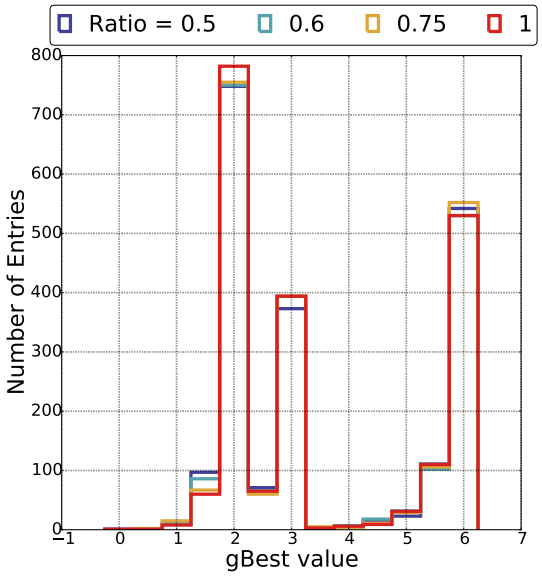

Simultaneous search with $D_c = 0.5$.

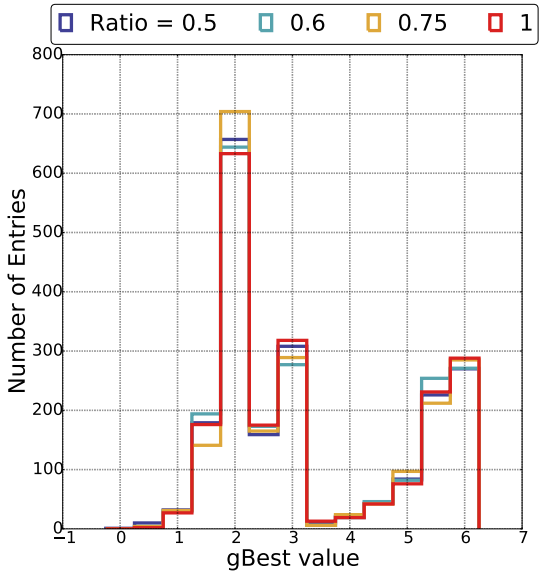

Simultaneous search without any distance constraint.

Figure 3.5: The figure shows that the performance of the hostile swarms is independent of the ratio of split of particles in the primary and secondary swarm. The simulation presented uses hostile swarms with an electrostatic repulsion potential between the sub-swarms to search an eight-dimensional parameter space with a total of 2400 particles.

Dimension	Np_{pso}		Dimension	Np_{pso}
2	200		9	2700
3	300		10	4000
4	400		11	5500
5	500		12	6000
6	600		13	6500
7	1400		14	7000
8	2400		15	7500

Table 3.1: The table summarizes the total number of particles used to sample the parameter space in N dimension. The boundaries are defined at (-5, 5) along any dimensional axis.

of particles in each sub-swarm by constraining the total number of particles in the hostile swarm search over N dimensions to be equal to Np_{pso}.

Figure 3.5 summarizes the performance of the hostile swarms algorithm in eight dimensions using a total of 2400 particles with different split ratios of particles in primary to secondary swarm. We have used an electrostatic ($1/r^2$) potential between the swarms for reasons which will become clear in the next section. From the figure, it is evident that the performance of hostile swarms variant is almost same and seems independent of the ratio of split as long as both swarms have a statistically significant number of particles to sample the parameter space.

3.4.2 Repulsion Potential

The choice of repulsion potential is crucial to the performance of the hostile swarms algorithm. The hostile swarms variant aims to improve performance and search the parameter space in a way that tries to ensure that particles of different sub-swarms do not end up exploring the same region of the parameter space. This idea is mimiced in a computationally simulated search with the use of repulsion potentials. Thus, the choice of repulsion potential significantly affects the performance of hostile swarms. We will explore the parameter space with two repulsion potentials – one linear with distance and the other which is electrostatic (1/r).

Figure 3.6 summarizes the results for all the possible search methods within hostile swarms with a linear repulsion potential between the sub-swarms, exploring an eight-dimensional parameter space with a total of 2400 particles. The number of particles in each sub-swarm is equal (split ratio = 1). We see that with linear repulsion the performance is poor, especially in higher dimensions.

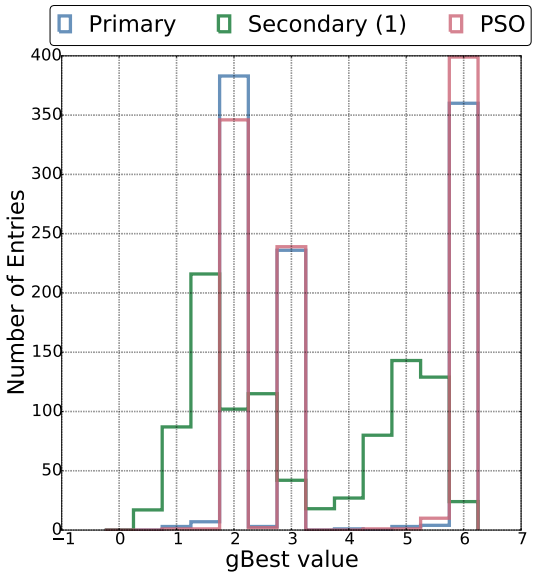

Relayed search with $D_c = 0.5$.

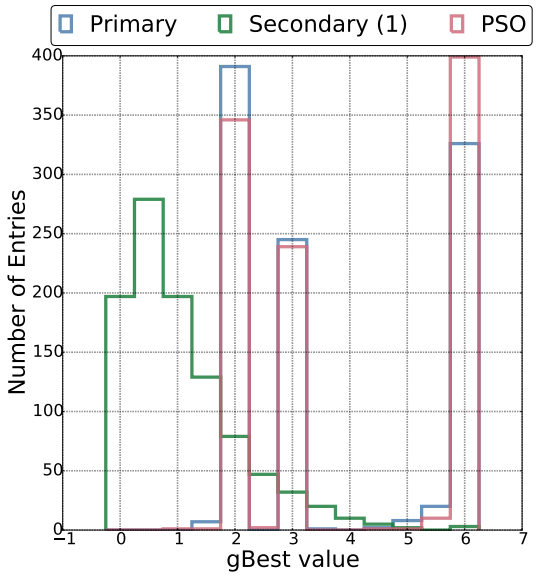

Relayed search without any distance constraint.

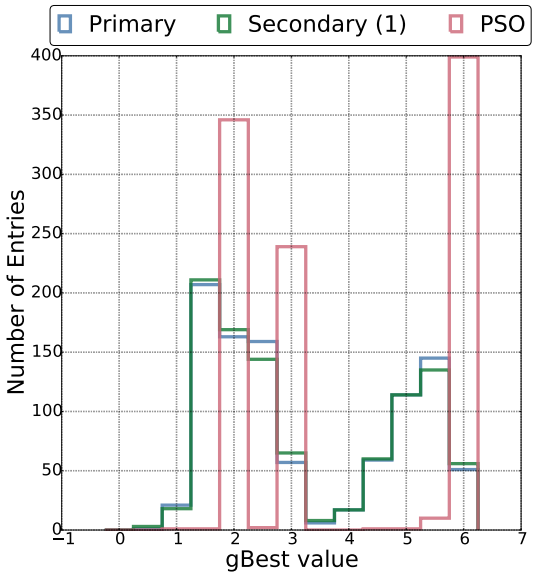

Simultaneous search with $D_c = 0.5$.

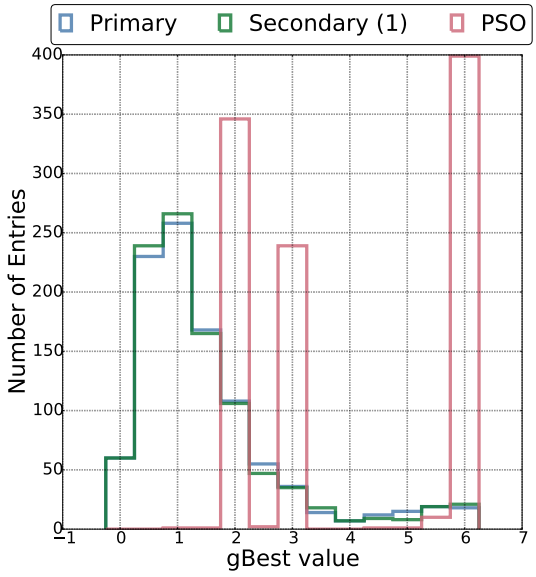

Simultaneous search without any distance constraint.

Figure 3.6: Simulations with a linear repulsion potential between sub-swarms while searching an eight-dimensional parameter space with 2400 particle. We see linear repulsion potential is a poor choice for higher dimensional spaces.

Note: The performance is acceptable for lower dimensional spaces, as we go to higher dimensions the performance degrades.

In the case of relayed search, the first swarm performs like a standard PSO search, but the performance of the second swarm is very poor. In the case of simultaneous search, both the swarms do not seem to perform optimization. Let us try to understand the reason for the under-performance. The answer is simple, the linear repulsion potential drives the swarms unstable. As the dimensionality of the parameter space increases, the maximum possible distance between two points in the parameter space increases and so does the average separation between the global best of swarm A and the particles of other sub-swarms. As the force in linear potential is proportional to distance, the force becomes so strong that particles do not converge but are kicked out of the search space and randomly reallocated. Thus, the swarm intelligence does not evolve and optimal solutions are not achieved.

The electrostatic potential serves the purpose well (figure 3.5) and will be used in the rest of our searches.

3.4.3 Search Methods in HPSO

Having justified the use of electrostatic repulsion potential and understood the effect of split ratios, we now proceed to compare the performance of the possible search methods, stated earlier, in hostile swarm optimization. As in earlier runs, we will use an eight-dimensional parameter space with 2400 particles equally divided into two sub-swarms which are hostile to each other. In figure 3.7, we plot the optimal solution found by each sub-swarm. We have also plotted the solutions obtained by using the standard PSO technique to allow comparisons.

1. Relayed search with a distance constraint D_c – The two swarms perform the job of optimization very well. There are a few cases of false peaks arising when the two sub-swarms converging to the same global optimal solutions. However, in these cases too, one of the two swarms holds the global optimal solution which can be checked for.

2. Relayed search without any distance constraint – As we neither have a distance constraint for possible global best attractors or the last few iteration steps of standard PSO, the instances of the second swarm converging to fictitious peak increases. Again this arises in a relayed search where the second sub-swarms ends up exploring the same region of parameter space

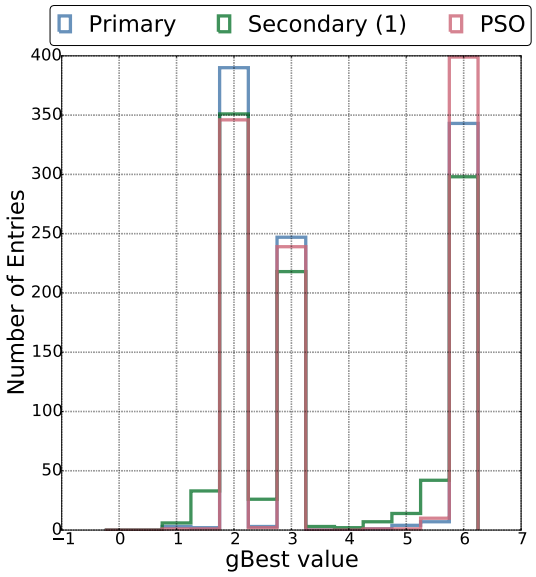

Relayed search with $D_c = 0.5$.

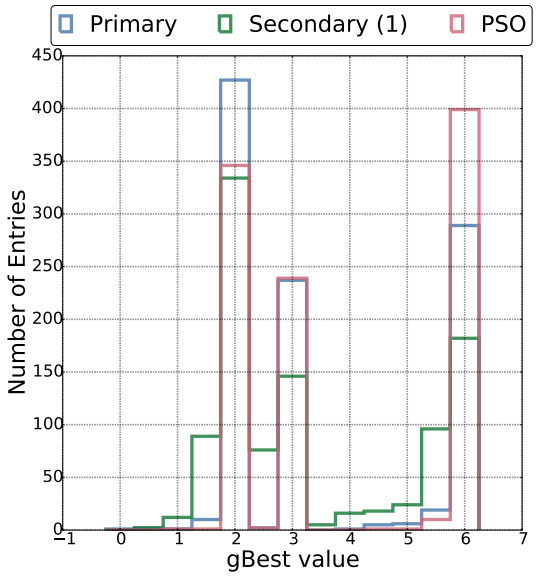

Relayed search without any distance constraint.

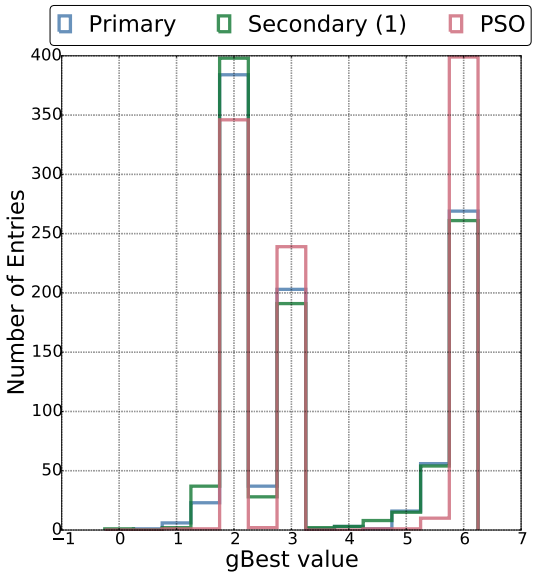

Simultaneous search with $D_c = 0.5$.

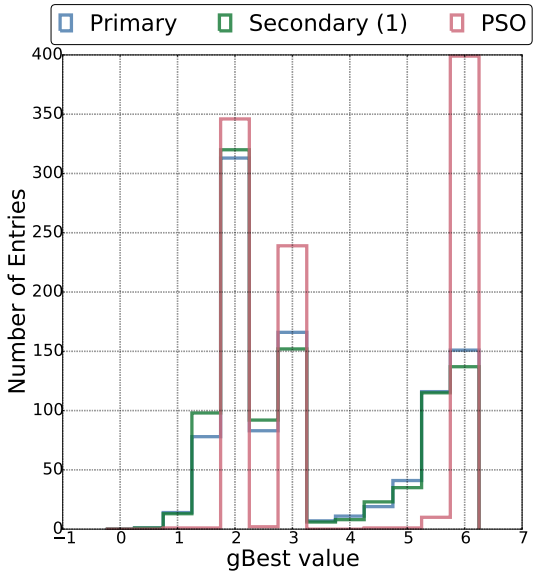

Simultaneous search without any distance constraint.

Figure 3.7: A comparison of the possible search methods with hostile swarms in an eight-dimensional search space. A total of 2400 particles are equally distributed between the two sub-swarms of hostile nature simulated by an electrostatic repulsion potential.

like the first swarm. Due to the repulsion force from the first swarm, the particles in the second swarm can not obtain the best possible location in that sub-domain.Thus forced to wander in contours around the global best of the first swarm.

3. Simultaneous search with a distance constraint D_c – The problem becomes a bit complicated in a simultaneous search. As the sub-swarms evolve at the same time, the global optimal solutions improve dynamically. As repulsion arises from the global best location at any point of time. The repulsion forces also change from step to step as global bests evolve giving rise to complicated sub-swarm interaction dynamics. When we constrain the possible distance, we force the swarms to look in other regions of phase space and avoid the chances of the global best attractor of two swarms to be the same. It is evident from the figure that this constraint gains importance in a simultaneous search where the global best attractor is changing iteratively. To further provide support to this hypothesis we see the unconstrained simultaneous search yields poor results.

4. Simultaneous search without any distance constraint – The method is not very effective as swarms start competing for global best location. Sometimes, the swarms end up close to optimal solutions without any one of the two converging to the optimal solution. In other cases, a situation similar to distance constrained simultaneous search arises where one of the swarm converges to the optimal solution and the other is forced to wander about it.

3.4.4 Improved efficiency of Global Optimum

We are now curious to see that does the hostile swarm method improve the chances of getting to the global optimum solution as compared to the standard PSO technique. The reason to ask this question can be understood by considering a case when one of the sub-swarm has converged to a local optimum and not global. The second sub-swarm will be repelled from this location and we wish to see does this lead to the global solution? To answer this question we do the following. If the sub-swarms converge to the same peak location, we remove one of the two and consider only one. This removal is done by calculating the distance between the global best location of the two swarms. If the peaks are separated by a distance less than one we remove the one with a lower global best value. Otherwise, we keep information of both the solutions. By doing so we have removed the common peaks.

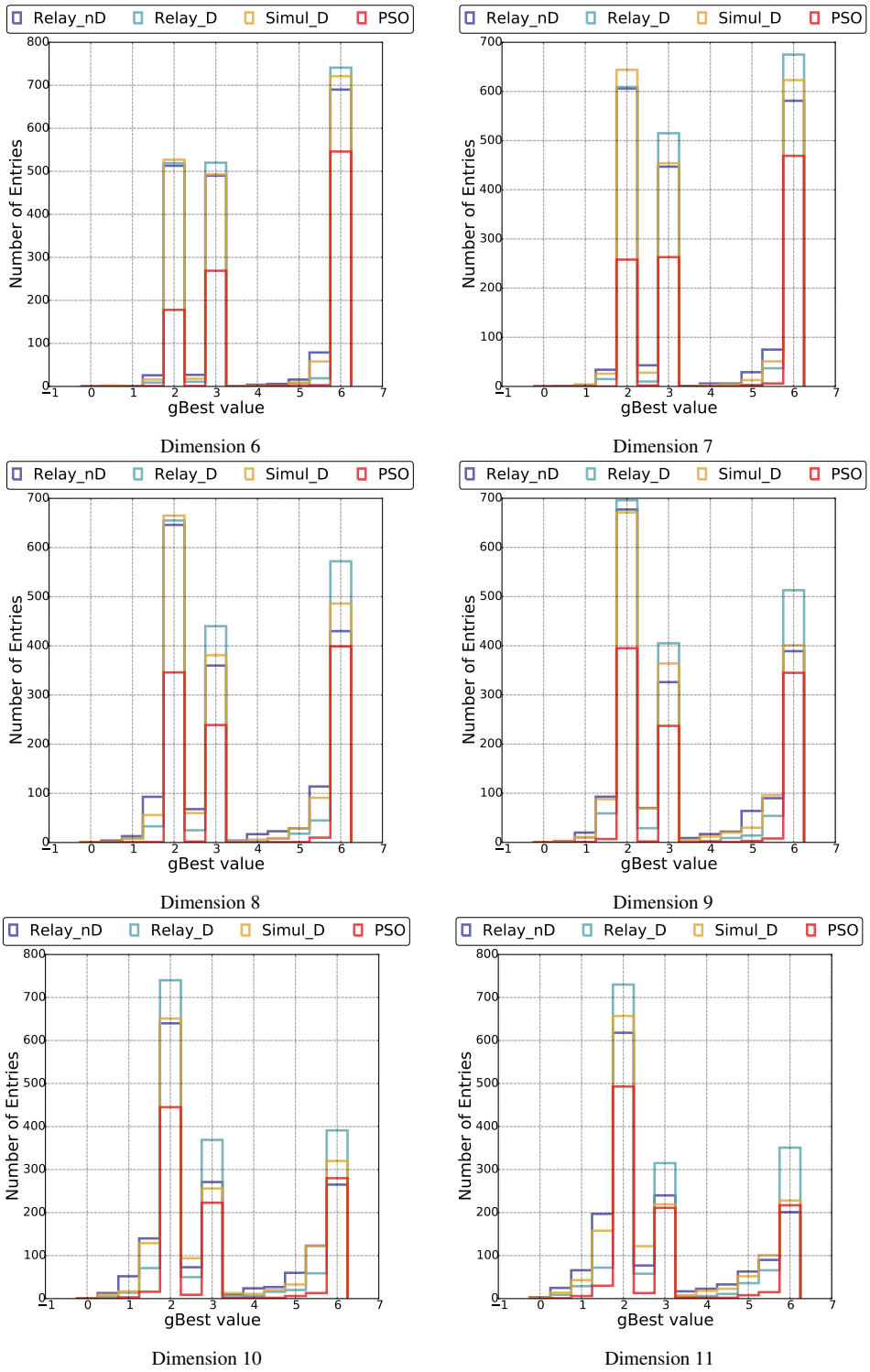

Figure 3.8: Comparing the performance of hostile swarm technique (after removing, if any, recurrent solution in a given trial) with PSO. We see with hostile swarm method provides an increased efficiency of exploring both the global and local optimal solutions.

Next, we combine all the non-recurrent peaks from the hostile swarms algorithm and the PSO. The result after removing the common peaks is plotted in figure 3.8. We see hostile swarm technique has an improved chance of detecting the global optimum compared to PSO, at the same computational cost. The trend is consistent with higher dimensions. Moreover, we see that there is a greater chance of the second sub-swarm to converge to another optimum solution. Thus, increasing the chance of getting both the global and optimal solutions. Thus making hostile swarm method a great tool to explore and study degenerate systems.

3.5 Discussions

We have shown that hostile swarms is a powerful method to find optimal solutions of a fitness function f in a given parameter space[1]. With an improved chance of exploring the global optimum solution as compared to the standard PSO. The method also yields local optimal solutions. This salient feature provides an upper hand when the system of interest has degenerate solutions. Moreover, if an optimal solution to a function is known apriori, relayed hostile swarm search method can be used to find other optimal solution to the problem, to check and gain confidence whether the known solution is indeed the global optimum or not.

[1]The project is completed and we are in the writing process.

Chapter 4

Detecting Gravitational waves using PSO

Particle swarm optimization is a very power algorithm to find optimal solutions in higher-dimensional space. We discussed in section §2.3.1 the parameters which influence the GW waveform from an astrophysical source can be as high as fifteen. To recover astrophysical signals from a noisy data stream and estimation the parameters of the astrophysical source is a computationally expensive job. Our project aims to use particle swarm optimization to reduce the computational burden in extracting the signal from noise. The use of PSO in GW data analysis was proposed by Wang and Mohanti (2010) [17]. Moreover, reduced cost implies lesser time to recover the signal and we could have a faster prompt system to notify the observatory collaborations across the globe to start looking for EM counterparts of the GW events. In our project, we also interested to estimate the parameters of the astrophysical source to considerable accuracy in the process of detection. This is crucial as EM counterparts from BH-BH mergers or extreme mass ratio NS-BH binaries are unlikely, if initial estimates are precise then the observatory will save the important time resource. With interesting results, the project is in progress and the future work aims to calculate the sky localization with PSO.

In this chapter, we will describe the methods and the parameter space used in section §4.1. We use a range of variants of the PSO to recover the GW signal. We will briefly describe these variants in section §4.2. We will motivate the study and present the results of different boundary conditions (BC) in section §4.3. Lastly, we will discuss the results of our simulations and compare the different variants of PSO used to recover the GW signal in section §4.4.

Parameter's	BH-BH binaries			NS-BH/NS-NS binaries		
	Non-spin	Low Spin	High Spin	Non-spin	Low Spin	High Spin
Mass m_1 ($M_\odot$)	20 - 80	20 - 80	20 - 80	1.4 - 20	1.4 - 20	1.4 - 20
Mass m_2 ($\leq m_1, M_\odot$)	20 - 80	20 - 80	20 - 80	1.4 - 10	1.4 - 10	1.4 - 10
Spin S_{1z}	0	-0.5 - 0.5	-0.85 - 0.85	0	-0.5 - 0.5	-0.85 - 0.85
Spin S_{2z}	0	-0.5 - 0.5	-0.85 - 0.85	0	-0.5 - 0.5	-0.85 - 0.85
Lower frequency cutoff (Hz)	20	20	20	20	20	20
Number of Injections	1000	1000	1000	1000	1000	1000
Waveform Approximant	IMRPhenomC Taylor3.5PN					

Table 4.1: Injection parameters in different search categories. All the signals which are injected have a SNR ≥ 8.

4.1 Approach

Our aim is to develop and test PSO algorithm to detect GW signals buried in noise. For the purpose, we generate N simulated injections in different mass and spin ranges. The injection parameters are grouped and summarized in table 4.1. All the injections generated and results are generating using the PyCBC software package [18, 19, 20]. As stated in section §2.3.1, to save computational cost, we consider binary systems with aligned or anti-aligned spins. We also add injections which have no GW signal, but only stationary gaussian noise. The reason for adding and searching over a time-series of noise is that any detection algorithm should not claim or trigger when there is just noise in the data stream.

Now let us consider an injection from an astrophysical source. To each such injection, we add white noise weighed by the PSD of the LIGO detectors. By doing so we have simulated data output from a GW detector which has signal buried in noise. The next job is to be able to detect this signal with the PSO algorithm. We will use PSO to optimize over the *Matched filter* and *Likelihood* functions discussed in section §2.3.5 and by doing so, we will try to hunt for the GW signal buried in noise. Our present work uses only one detector data. As a result, localization studies are not included. Lastly, we will use the standard (for a single detector) SNR threshold of 8 to flag any event as a successful detection. The dimension of our parameter space is six, as a result, linear repulsion potential is effective to sample the paramter space.

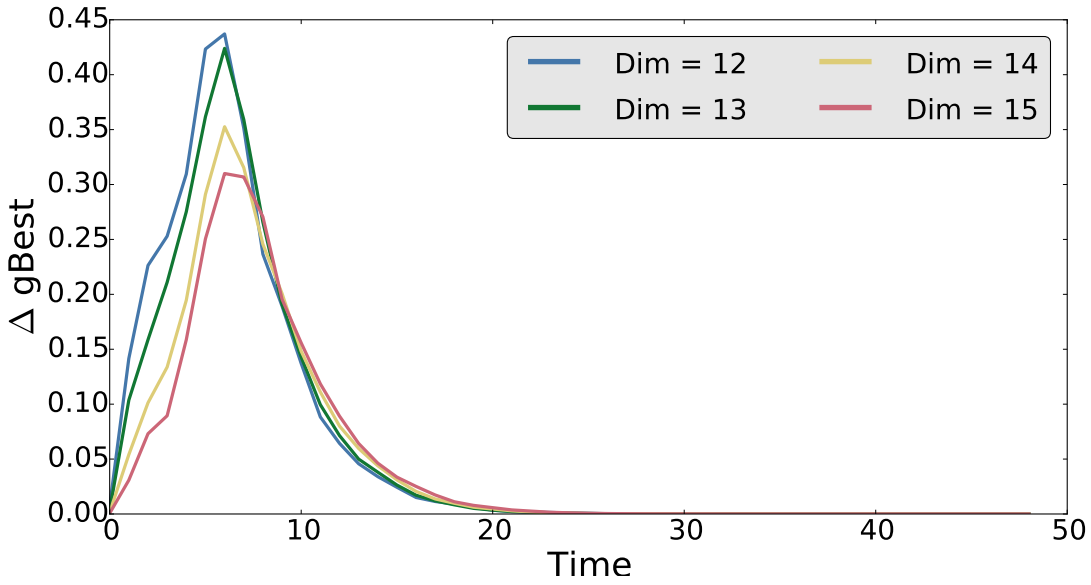

Figure 4.1: The figure shows the average change in global best location averaged over 1000 trials as a function of time. We see in later iterations the global best barely changes.

4.2 Variants of PSO

We use the standard PSO algorithm described in section §3.1 and its extension to multiple independent swarms described in section §3.2. We use the hostile swarms algorithm §3.3 with both linear and electrostatic potential. Lastly, a variant of PSO useful particularly to GW data analysis is described below.

4.2.1 Remove PSO

The process of matched filtering a single template with a data stream is computationally expensive. It involves a cross-correlation with data which can be few hundreds to thousands of seconds long. Thus, at each step evaluation of the match or likelihood function is costly. In remove PSO we use a simple trick to reduce this cost. The method will be useful in cases where the cost of evaluation of the fitness function is costly.

PSO algorithm is a quick method to find optimal solutions of a given function (fitness function). When evolved over N iterations the swarm of particles eventually converges to an optimal loca-

tion in the parameter space. However, when the swarm has converged, in successive iterations the particles explore and wander close to the gBest, thus the gBest value remains constant on changes slightly during the later stages. The figure 4.1 shows the evolution of gBest over successive iteration averaged over 1000 trials.

When the cost of evaluation of the fitness function is high, the later steps which do not improve the gBest significantly can be compromised to save time. Thus, we can remove the particles from the swarm at later stages without affecting the swarm's efficiency to explore the gBest. Consider a total of N iterations were allowed for the swarm to evolve. However, in order to save time, we choose to remove particles after M (<N) iterations. The removal of particles can be done in two ways described below.

1. Removing the converged particles – After M iterations, we construct a box around the gbest or hypersphere of radius r centered at gBest. Next, we remove a fraction f of the particles which lie within this volume.

2. Removing the grouped particles – We divide the parameter space $(d_1, d_2, d_3....)$ in $(n_1, n_2, n_3....)$ bins. Be doing so we have divided the parameter space in grids. After M iterations, remove a fraction f of the particles which lie in the same hyper-grid.

We will compare the performance of all the variants of PSO in the last section of this chapter.

4.3 Boundary Conditions

Boundary conditions serve the purpose of re-spawning the particle, in cases when after successive iterations, the particles leave the parameter space under survey. Sometimes particles may simply enter regions of parameter space which are not of interest. Other times the problem becomes more complicated when the particles fly into unphysical regimes, parameter values are unrealistic and not in accord with the fundamental principles of physics. BCs are used to overcome these problems in simulation. The choice of BCs to use in a given system is important to a uniform sampling of the parameter space.

In PSO particles may have high velocities in the initial steps and points close to the boundaries may be undersampled due to this reason. To elaborate consider a one-dimensional space with boundaries (-5,5) with the solution located close to the boundary. With the velocity of a particle

BC	Detection efficiency (SNR $\geq$ 8)	Relative $\Delta M_{Chirp}(\%)$		Relative $\Delta Q(\%)$		$\Delta \chi_{eff}$	
		Mean	Sigma	Mean	Sigma	Mean	Sigma
Rand	0.939	-4.98	10.95	43.27	44.02	-0.039	0.178
Ref	0.943	-5.31	11.66	44.36	40.74	-0.044	0.195
StoRef	0.935	-5.42	11.40	43.31	38.05	-0.049	0.200
Moving (p = 0.50)	0.943	-4.83	11.55	41.77	40.55	-0.036	0.188
Moving (p = 0.75)	0.935	-4.54	10.97	40.74	39.72	-0.033	0.176
Moving (p = 0.90)	0.944	-4.92	11.45	41.90	42.36	-0.038	0.188

Table 4.2: Detection efficiency and errors in source parameter estimation for different boundary conditions used, when all the 1000 injections are forced near the boundary. All the signals are injected with an SNR $\geq$ 8. The table summarizes the mean and standard deviation in the error estimation of the parameters – chirp mass, the mass ratio and effective spin parameters.

being high it is likely they will overstep the boundary, eg from 3 to 7, thereby undersampling the regions near the boundary. We use multiple BCs, to figure out which is possibly the best candidate in our case. The different BCs we use are described below.

1. Random Uniform Re-spawning (*Rand*) – During the course of evolution, any particle which escapes the parameter space is randomly put back in the parameter space with a prior using a uniform distribution.

2. Reflecting (*Ref*) – Particles which are flying out of the boundary are instead reflected back into the parameter space.

3. Stochastic Reflecting (*StoRef*) – The reflection is like a scattering process. Particles which are flying out of the parameter space are reflected stochastically. By adding a stochastic term – a random number between 0 and 1, determining the magnitude of reflection is used. This is done with the aim to sample more points near the boundary.

4. Moving (*Moving*) – We allow a probability p for the points to be outside the parameter space. If the particle is lucky it can wander away. Otherwise, it is respawned in the parameter space with the random uniform respawning method.

To compare the performance of the various boundary conditions, we force all the injections near the boundary with Q value in the range [1, 1.1]. The injections are Low Spin BH-BH injections (see table 4.1). We use two independent swarms with hundred particles each to recover these injections with likelihood maximization. The comparison between the different BCs discussed above is summarized in table 4.2.

BC	Detection efficiency (SNR $\geq$ 8)	Relative ΔM_{Chirp}		Relative ΔQ		$\Delta \chi_{eff}$	
		Mean	Sigma	Mean	Sigma	Mean	Sigma
Rand	0.975	-2.79	18.94	11.50	44.04	-0.044	0.33
Ref	0.963	-3.60	18.75	14.48	49.90	-0.050	0.34
StoRef	0.961	-3.31	18.04	12.87	47.84	-0.045	0.32
Moving (p = 0.50)	0.961	-3.24	18.14	8.54	45.48	-0.048	0.32
Moving (p = 0.75)	0.973	-3.36	18.58	12.55	48.66	-0.047	0.33

Table 4.3: Detection efficiency and errors in source parameter estimation for different boundary conditions used, when the 1000 injections are uniformly smeared in the parameter space defined in the low-Spin BH-BH binaries category in table 4.1. All the signals are injected with an SNR $\geq$ 8. The table summarizes the mean and standard deviation in the error estimation of the parameters – chirp mass, the mass ratio and effective spin parameters.

We see the detection efficiency is comparable among the various BCs used. However, the way they estimate the parameters and thus the estimation of errors by each method is more significant. We find the Moving BC with p = 0.75, implying that particles have a 75% chance to remain outside the parameter space. We see by increasing this probability further the efficiency decreases, which is expected as the number of particles sampling the parameters space of our interest reduce.

One should note that this discrepancy in performance arises when injections are forced near the boundary. If the injections are smeared uniformly in the parameter space, the performance between different BCs is summarized in table 4.3. We find the random respawning and moving BC with a fifty percentage chance for the particles to fly away perform well. The latter outperforms the other in the estimation of Q values. The detection efficiency between different BCs is again comparable.

4.4 Results and Discussion

We will now compare the detection efficiency and the estimation efficiency of different variants of PSO. One should note that in a template bank search, the templates are placed with a mismatch of 3% compromising accuracy to reduce computational cost and increase speed [21]. This mismatch translates to approximately 10% loss in detection efficiency.

We will use the variants of PSO to find a global optimal solution of the matched filter function and the likelihood function. We will present the results for the BH-BH binary and NS-NS/NS-BH binary in the following subsections.

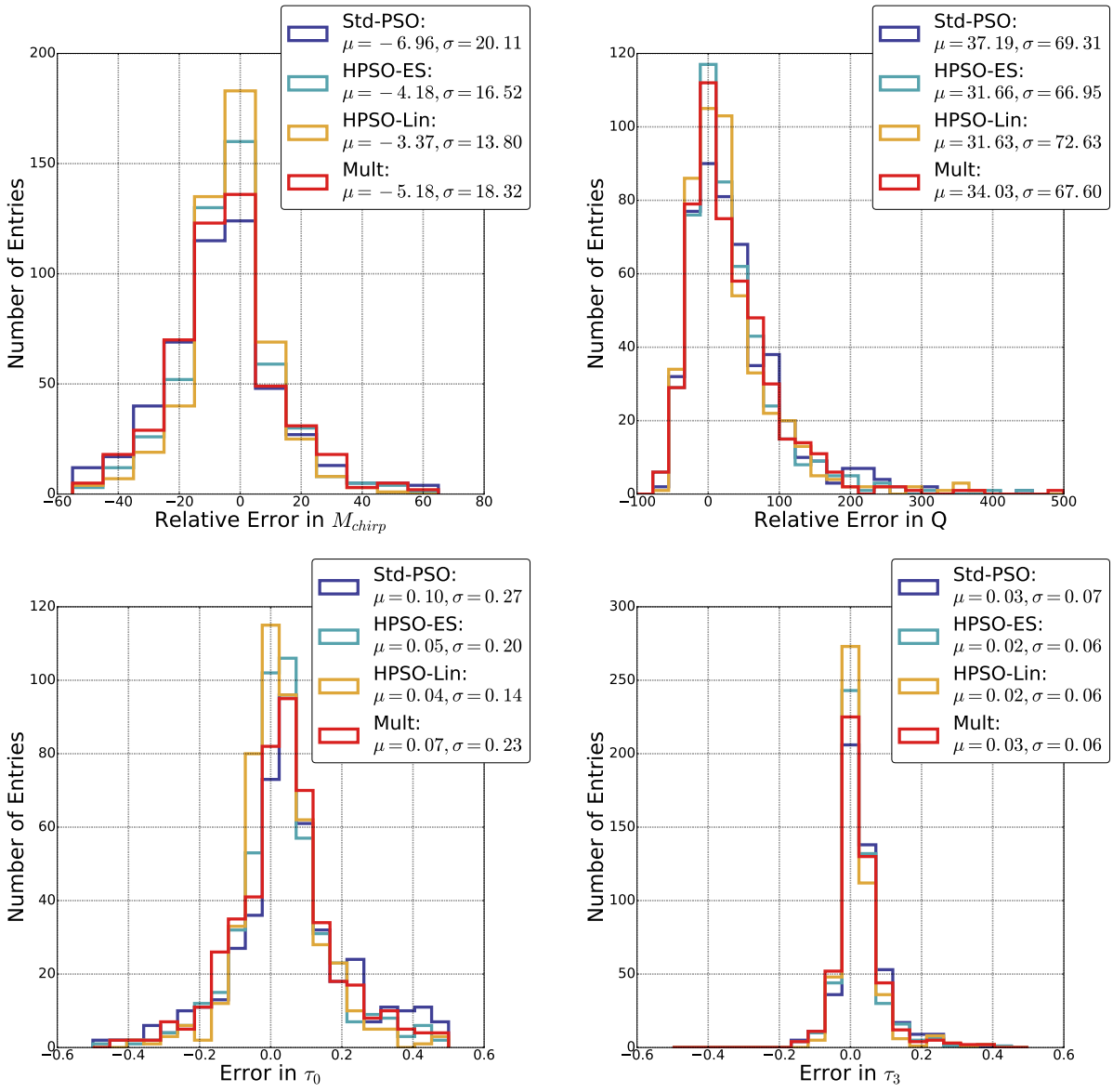

Figure 4.2: Comparing different variants of PSO (using a total of 400 particles) from their efficiency to estimate source parameters from likelihood optimization to recover high-spin BH-BH injections.

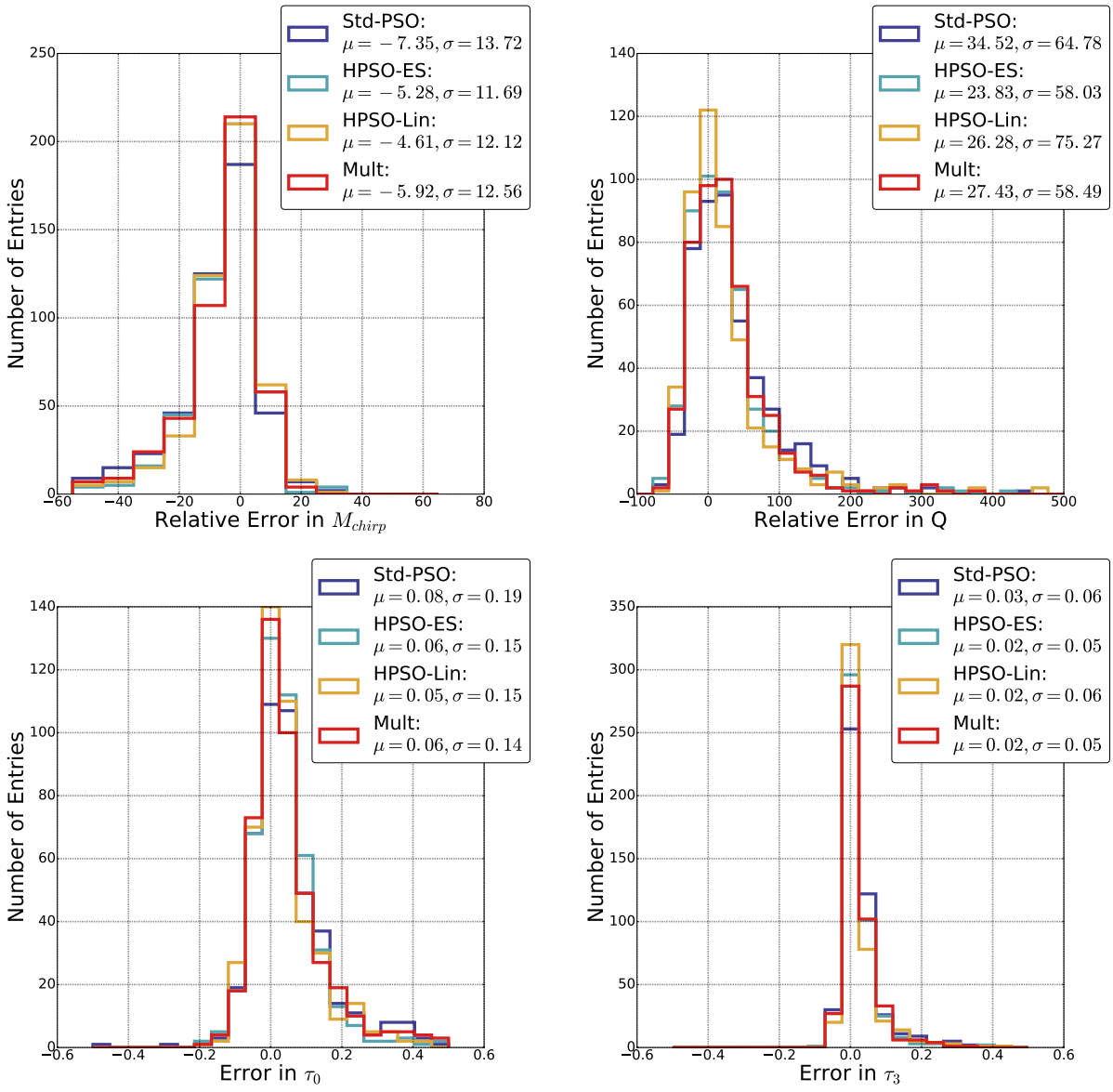

Figure 4.3: Comparing different variants of PSO (using a total of 400 particles) from their efficiency to estimate source parameters from likelihood optimization to recover low-spin BH-BH injections.

PSO Variant	Detection Efficiency (SNR $\geq$ 8)	
	High Spin BH-BH	Low Spin BH-BH
Standard PSO	0.951	0.947
Hostile Swarms - ES	0.965	0.955
Hostile Swarms - Linear	0.967	0.965
Multiple Independent	0.965	0.955

Table 4.4: The table summarized the detection efficiency of different variants of PSO surveyed. The search is done using the likelihood function as the fitness function. All the signals are injected with an SNR $\geq$ 8.

4.4.1 BH-BH binary

For BH-BH binary systems, both the likelihood optimization and matched filter optimization yield similar results. The latter outperforms in the number of successful detections, while the former provided better first hand estimated to the source parameters. We keep the total number of particles used in any variant as constant. This is done to ensure each variant takes the same computational cost to detect and estimate the parameters. Using data from the single detector, we search over six parameters – masses, aligned spins, distance, and inclination. We use a total of 400 particles to recover the BH-BH binary signal embedded in stationary gaussian noise. However, the detection efficiency is almost same for 200 particles. We choose the random uniform respawning (Rand) BC in all the simulations.

We have broken the parameter space of BH-BH binary into two – high spin binary systems and low spin binary systems. The detection efficiency of different variants for each is summarized in table 4.4. The error in estimation of the chirp mass, the mass ratio(Q) and coalesce time (τ_0, τ_3) for high-spin BH-BH binary system and low-spin BH-BH binary system, from likelihood optimization, are shown in figure 4.2 and 4.3 respectively.

We see that although the different variants had similar performance in triggering a successful detection. However, the corresponding error in parameter estimation in each is quite different amongst the variants. We see that the hostile swarms with linear repulsion potential performs slightly better than hostile swarms with electrostatic potential, which in turn, perform better than standard PSO.

Detection Efficiency (SNR $\geq$ 8) – NS-BH/NS-NS				
PSO Variant	Likelihood Optimization		Matched Filter Optimization	
	High Spin	Low Spin	High Spin	Low Spin
Standard PSO	0.699	0.834	0.920	0.960
Hostile Swarms - ES	0.742	0.853	0.916	0.968
Hostile Swarms - Linear	0.764	0.840	0.938	0.971
Multiple Independent	0.702	0.836	0.924	0.954

Table 4.5: The table summarized the detection efficiency of different variants of PSO surveyed. All the signals are injected with an SNR $\geq$ 8.

4.4.2 NS-NS/NS-BH binary

The picture and results drastically change for a NS-NS/NS-BH search. The detection efficiency and parameter estimates vary drastically between the likelihood and matched filter optimization. We increase the number of particles used to 600 to better sample the parameter space. The other search tools – BCs, dimension, etc are similar to BH-BH binary search. The detection efficiency for NS-NS/NS-BH binary system for both likelihood and matched filter optimization is summarized in table 4.5. The plots 4.4, 4.5 and 4.6, summarize the errors in the estimation of parameters in the case of likelihood optimization over low-spin NS-NS/NS-BH injections, matched filter optimization over low-spin and high-spin NS-NS/NS-BH binaries respectively. The error in the estimation of the effective spin parameter in different injection sets is collectively summarized in figure 4.7

From the plots, it is clearly evident that, in NS-NS/NS-BH binary search, the performance of different variants of PSO has improved when the matched filter optimization is used. Thus, making PSO and its variants a promising algorithm for developing quick detection pipelines which may make it easier for the telescopes across the globe to find and EM counterpart of a GW trigger.

4.5 Future Work

We will now extend our search for a network of GW detectors and aim to obtain the sky localization errors with PSO.

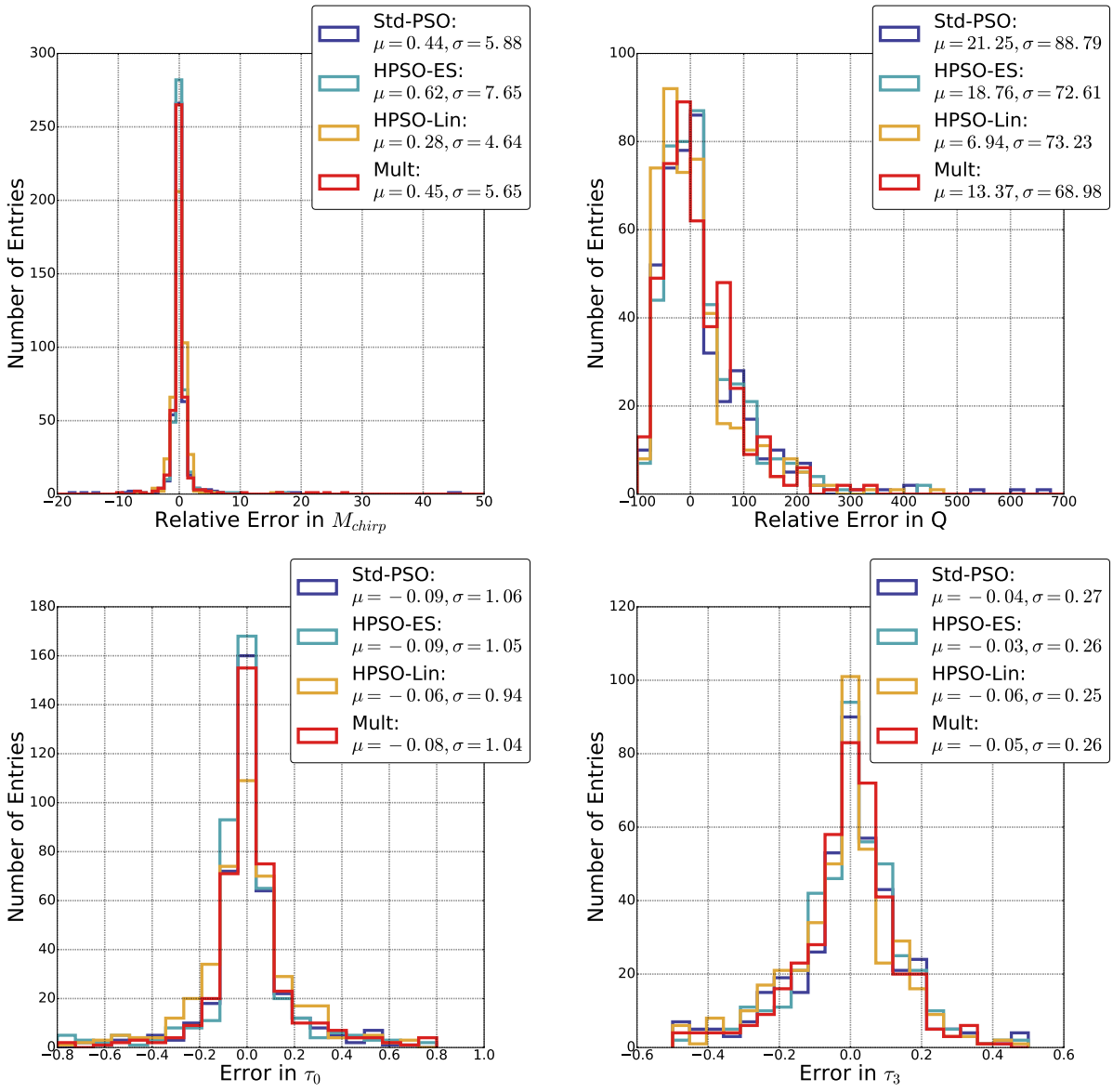

Figure 4.4: Comparing different variants of PSO (using a total of 600 particles) from their efficiency to estimate source parameters from likelihood optimization to recover low-spin NS-NS/NS-BH injections.

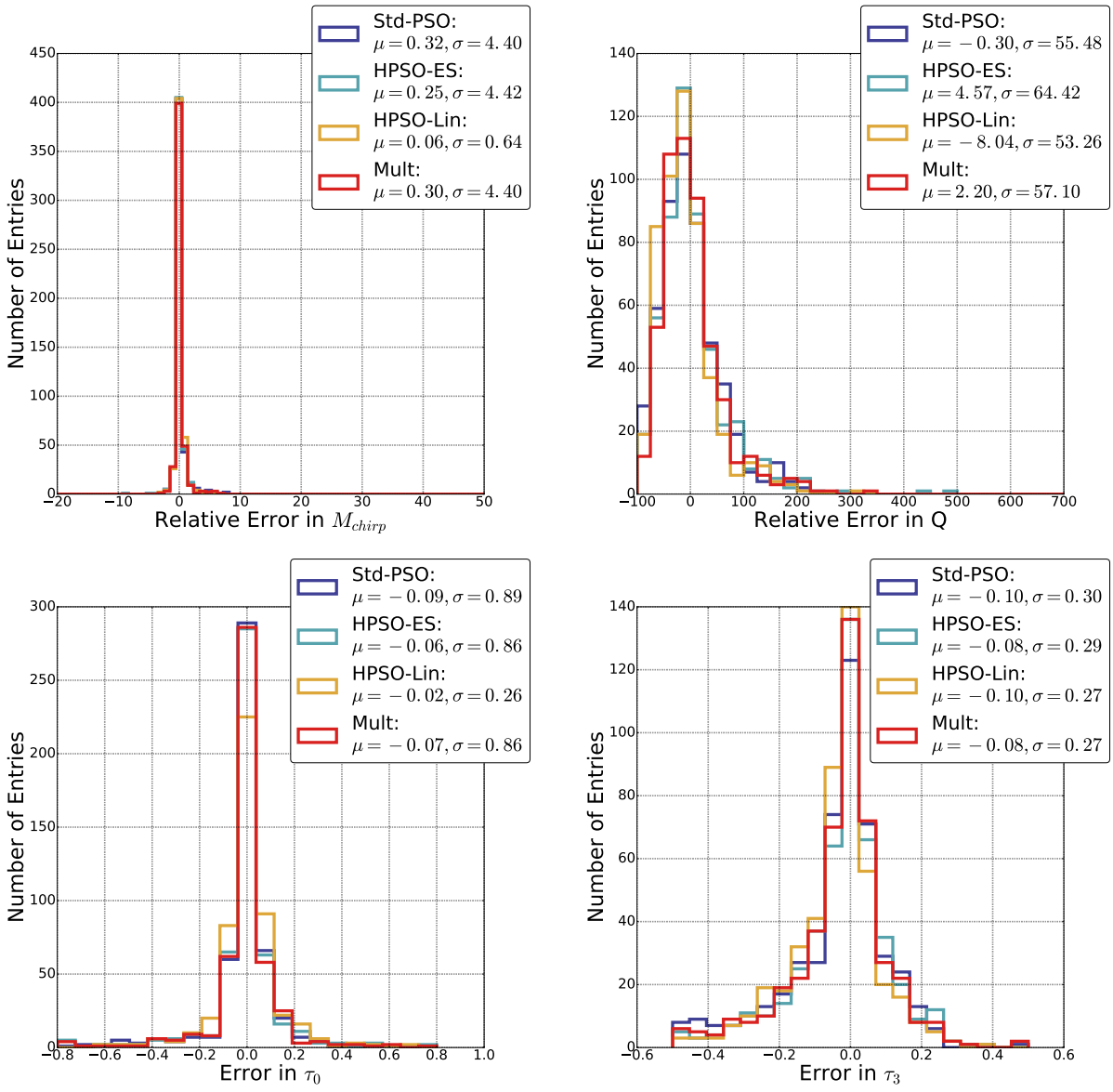

Figure 4.5: Comparing different variants of PSO (using a total of 600 particles) from their efficiency to estimate source parameters from matched filter optimization to recover low-spin NS-NS/NS-BH injections.

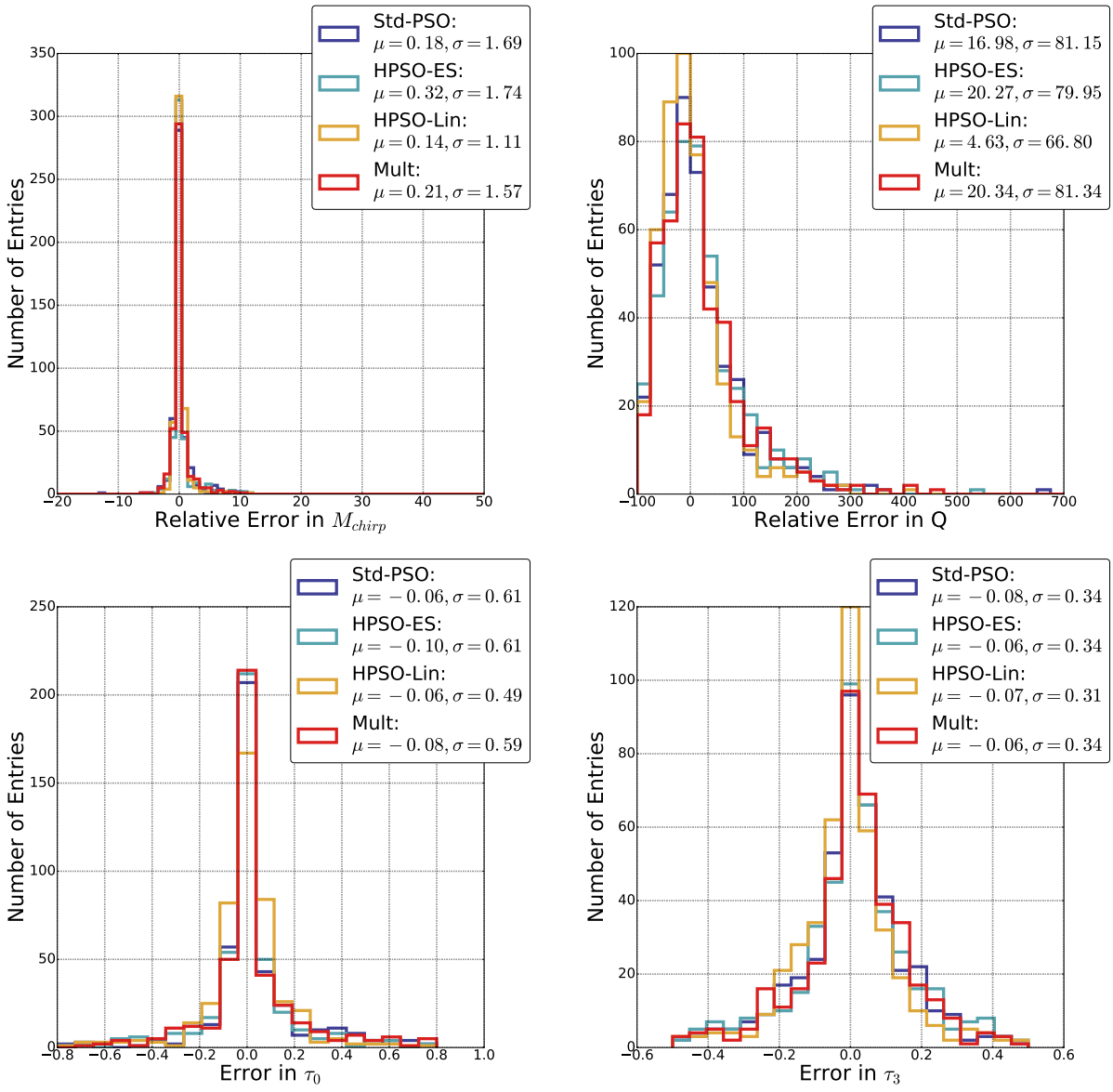

Figure 4.6: Comparing different variants of PSO (using a total of 600 particles) from their efficiency to estimate source parameters from matched filter optimization to recover high-spin NS-NS/NS-BH injections.

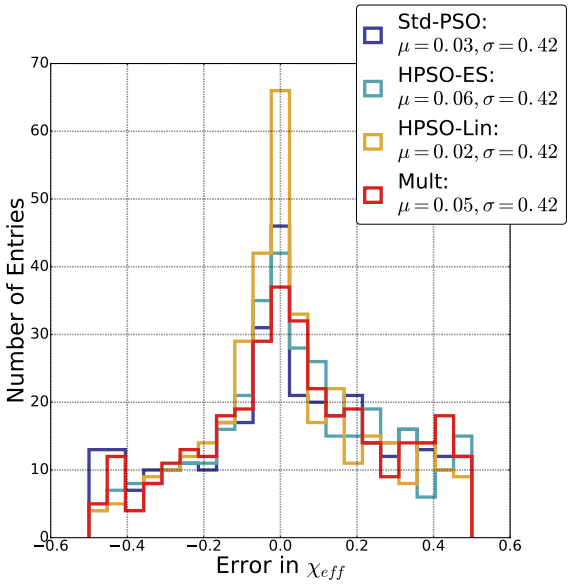

Matched filter optimization to recover high-spin NS-NS/NS-BH injections.

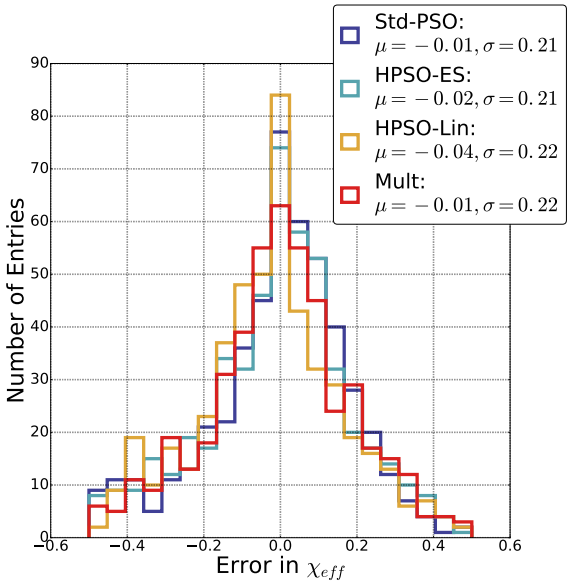

Matched filter optimization to recover low-spin NS-NS/NS-BH injections.

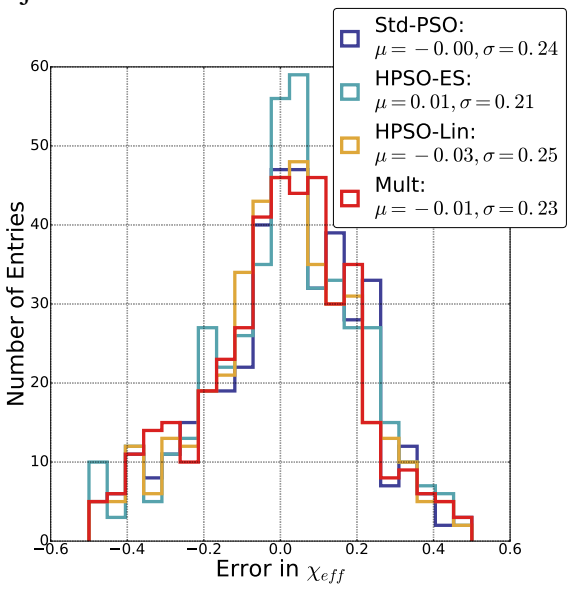

Likelihood optimization to recover low-spin NS-NS/NS-BH injections.

Figure 4.7: Estimation of χ_{eff}

Chapter 5

Geographic and Annual Influences on Optical Followup of Gravitational Wave Events

In §1.5 we discussed the motivation and challenges in the EM follow-up of GW events detected by LIGO. The LIGO-VIRGO GW detectors all have an antenna like all-sky sensitivity. If one consider a network of GW detectors which successfully detect a given astrophysical event. A network of two detectors has poor localization capability, a typical localization size is of the order of hundreds of square degrees. The accuracy to localize the source improves with increasing the number of detectors. This is a motivation for the IndIGO project. Moreover, the localization efficiency depends on the location of the source in the sky [4], figure 5.1.

We motivate our project with the question that do the discrepancies in the localization efficiency in different regions of the sky translate to some locations on the globe being better sites for optical telescopes. The "good" location is also dependent on the timing of the LIGO science runs. For example, consider the LIGO detectors are operational during the northern winters. Then the northern hemisphere observatories will have a longer time duration available to observe the localization patch. In our study, we will consider these two factors and see how do they affect the EM-followup capabilities of various observatory sites.

We will explain our approach and methodology used in the analysis in section §5.1. The effect of timing of LIGO-VIRGO runs is discussed in section §5.2. The results for the timing of LIGO runs

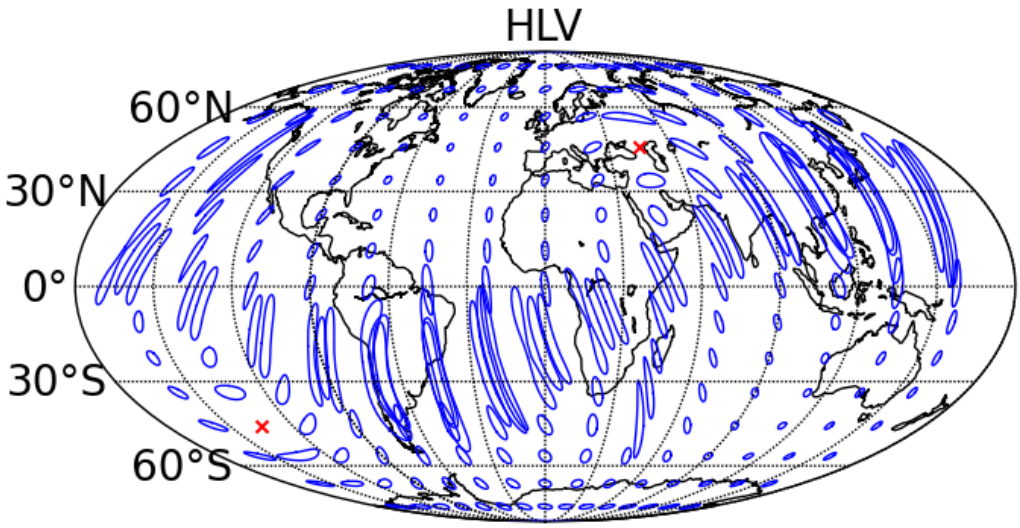

Figure 5.1: Using the time of arrival information to localize the source in the sky, the blue ellipses represent the 90% localization area in the sky. The red crosses are the blind spots of the detector network. The plot uses the O2 (2017-2018) detector sensitivity to localize the sources in the sky. [4]

are presented in §5.3. Lastly, we will conclude with the implications of our study in section §5.4. For a more detailed study kindly refer to the published article [22].

5.1 Method

Our interest is to study the effect of (1) site location and (2) the timing of LIGO-VIRGO science runs, on the probability of finding EM counterparts from GW events. For the reason, it is very important to set aside telescope capabilities from location. As we want to compare sites, we do not consider telescope parameters like – field of view, exposure time, telescope downtime, etc. We make the assumption that any given site across the globe has a capability to cover N sq. deg. of the sky. Then the question which site is favourable or better for EM follow-up of GW events can be translated to "Given each site can cover N sq. deg. , then which site on an average has a greater probability of finding an EM counterpart?". To answer the question, we simulate the EM follow-up of GW events independently from each site taken in our survey.

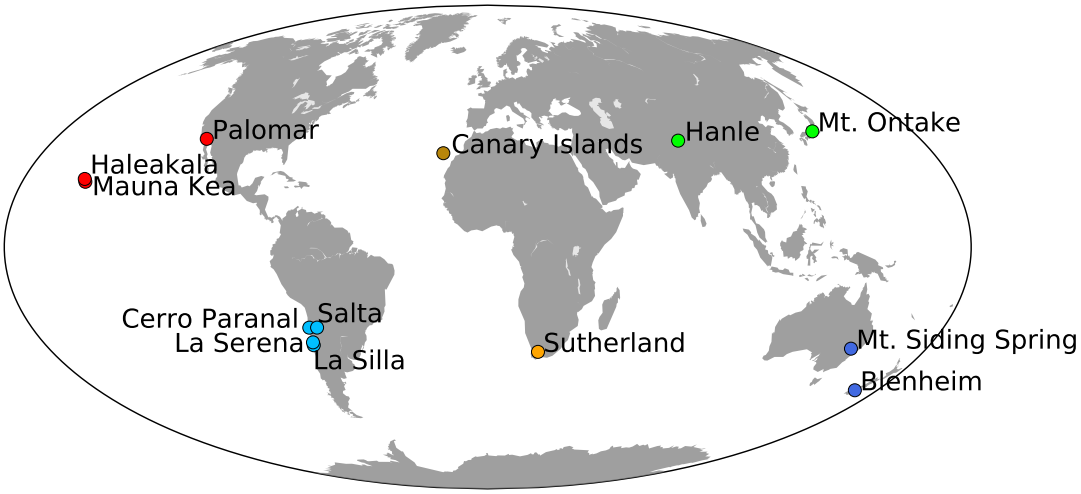

Figure 5.2: The locations of the Optical-Infrared ground-based observatories which took part in the EM-followup of GW150914 event. We have added Hanle as a representative observatory in Asia.

As discussed in section §1.5, the NS-NS mergers are theoretically unconstrained. A number of model varying in physical consideration and the proposed mechanism of the evolution of ejecta arising from a NS-NS merger. The EM signal arising from NS-NS/NS-BH merger is termed as kilonova. Different models predict different timescales for kilonovae transient signal. Several models [23, 24, 25, 26, 27] predict a kilonovae transient evolving on a timescale of a day or more. For these models, the transients evolve slightly during successive days, the first twenty-four hours following the trigger is a good representative of the entire event of EM followup. Moreover, for models evolving on timescales of a day, the sub-day responses loose significance. In our analysis, we do not consider the time delay(sub-day response) between the time when the signal arrived (detected by the GW detectors) and the first possible EM observation. This delay is corresponding to the time taken to ensure the signal in the detector is attributed to an astrophysical source and not to a machinery artifact.

5.1.1 Site Selection

For our survey, we choose the locations of ground-based optical observatories which took part in the follow-up of GW150914 [28]. We have added Hanle, India - site for the upcoming 0.7 m telescope purely dedicated to EM follow-up through the GROWTH project. These locations are shown in figure 5.2 and the corresponding details are summarized in table 5.1

5.1.2 Simulated GW Events

We use the GW localizations released by Leo P. Singer et al (2014) [29]. These GW localizations are obtained by simulating NS-NS binaries and then using proposed detector sensitivity of LIGO-Hanford(H), LIGO-Livingston(L) and VIRGO(V) during the LIGO-O1 phase and LIGO-O2 phase, they try to detect the GW signal from these NS-NS binaries. Any binary is considered as successfully detected only if the surpasses the pre-defined detection thresholds like SNR. The sky localization is calculated using `BAYESTAR` [30] and is available for public access in form of `HEALPix` files. The released set of patches comprises of 630 events recovered with HL detector network at O1 sensitivity. The O2 release comprises of 365 HL, 15 HV and 14 LV events along with 81 events recovered with HLV network at O2 sensitivity. However, these simulated detections are done assuming the detectors are operational during the period from 18 August to 19 October, during both the O1 and O2 detector data acquisition runs. This is not consistent with the actual observing run O1 and the expected dates for O2. The date stamp of the localization must be changed before we can study the geographic and annual influences.

The area of localization in the sky, as stated earlier, depends on the sensitivity of the GW detectors in the direction of the source in the sky. For example, any source detected if located above South America will be poorly localized compared to a source above North America, figure 5.1. The GW detector sensitivity is fixed in the geocentric coordinate system. Implying that any source localization recovered with a network of GW detectors on a given day and time can be mapped to a different day and time, as long as the relative orientation of the geocentric (detector) and celestial (source) coordinate is the same. That is, we can map and shift the dates as long as the sidereal time is invariant under the transformation. In our analysis, all transformations of the localization released in [29], to different dates ensure that the sidereal time is invariant. For the O1 observing run, we uniformly distribute all the simulated events in the period between 12 September 2015 to 19 January 2016. For O2, we split the observing period into two parts – O2A and O2B. During

Site	Telescope/Instrument	Latitude	Longitude	Altitude	URL
Blenheim, New Zealand	BOOTES-3	45° S	169° 41′E	27 m	http://bootes.iaa.es/en/
Mt. Siding Spring, Australia	Skymapper	31° 16′S	149° 04′E	1163 m	https://en.wikipedia.org/wiki/Siding_Spring_Observatory
Sutherland, South Africa	MASTER-SAAO	32° 17′S	20° 18′E	1760 m	http://observ.pereplet.ru
La Serena, Chile	DECam (CTIO)	30° 10′S	70° 48′W	2207 m	http://www.ctio.noao.edu/noao/
La Silla, Chile	TAROT-LaSilla	29° 15′S	70° 43′W	2400 m	http://tarot.obs-hp.fr/infos/
Cerro Paranal, Chile	VST	24° 37′S	70° 24′W	2600 m	http://www.eso.org/public/teles-instr/
Salta, Argentina	TOROS	24° 36′S	67° 19′W	4650 m	http://toros.phys.utb.edu/
Mauna Kea, Hawaii	W. M. Keck	19° 49′N	155° 28′W	4145 m	http://www.keckobservatory.org/about/
Haleakala, Hawaii	PanSTARRS	20° 42′N	156° 15′W	3052 m	http://neo.jpl.nasa.gov/programs/
Canary Islands, Spain	Liverpool	28° 45′N	17° 52′W	2363 m	http://telescope.livjm.ac.uk/About/
Hanle, India	Hanle	32° 47′N	78° 52′E	4500 m	http://www.iiap.res.in/iao_site
Palomar, USA	PTF	33° 21′N	116° 51′W	1712 m	https://en.wikipedia.org/wiki/Palomar_Mountain
Mt. Ontake, Japan	Kiso	35° 47′N	137° 37′E	1130 m	http://www.ioa.s.u-tokyo.ac.jp/kisohp/TELS/tels_e.html

Table 5.1: Details of observatory locations that took part in the follow-up of GW150914 event.

O2A, we consider only HL detectors as operational during the period spans from 1 December 2016 to 28 February 2017. During O2B, we consider all three detectors HLV operational in the period from 1 April 2017 to 31 May 2017. We emphasize the dates for O2 are tentative.

We will from now on use the term "patch" in further discussion, which stands for the 99% credible localization region. To study the effect of location in follow-up, we shift all the simulated GW events to the day of equinoxes – each location has the same amount of time available to observe the patch. We also shift all the simulated GW events to the day of summer and winter solstice – an estimate of the maximum possible annual variation. Results from these simulations are discussed in section §5.2.

5.1.3 Analysis

We use `Astropy` and `Healpy` to analyze the patches. We allow a time period of twenty-four hours from the trigger time for the observations to be recorded by each site independently. One important note: *as we have chosen a time period of twenty-four hours from the trigger, our analysis is not valid for kilonovae transients with a timescale of few hours*. Any region of the patch is qualified to be observable if the following conditions are satisfied

1. *Horizon* $\geq$ *24* $^\circ$: Any part of the patch can be observed only if it is 24° above the horizon. This constraint is put for two reasons. One, the telescope cannot point arbitrary close to the horizon, instrumentally not possible. Second reason is more of a quality check parameter. Pointing close to parameter means the light/signal from the source has to travel a greater path length. The light is scattered significantly and image quality degrades. To ensure good image clarity this constraint is followed by many ground-based observatories.

2. *Twilight* : Any part of the patch is observable only if it the sun is 18° below the horizon. In layman terms this constraint implies that it must be dark enough at night before the observatory can open its dome to start observations.

From each given patch we simulate the event of followup and select the `HEALPix` pixels satisfying the above conditions. The we sort the pixels in decreasing order of probability of having an EM counterpart. Then we sum the probability in the first N sq. deg. tiles, where N = 1, 3, 10, 30, 100, 300, 1000, 3000 sq. deg. We choose 3000 sq. deg. as an upper bound because typically, for events localized using a two GW detector network vary in size from a few tens to a few thousands of

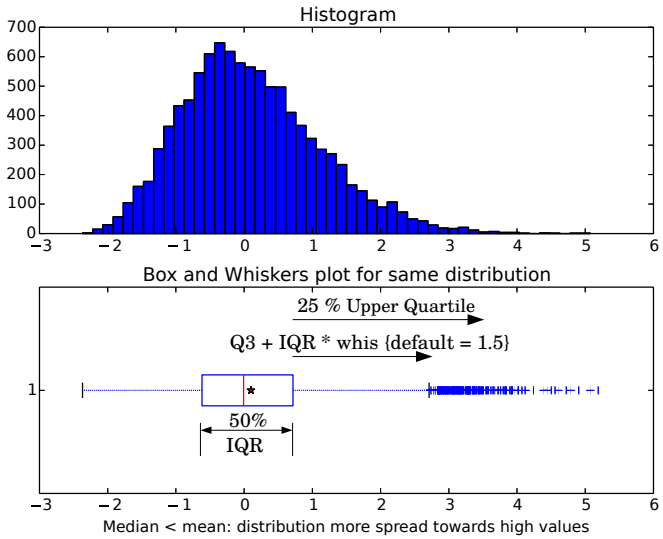

Figure 5.3: A box and whiskers plot for a given histogram plot.

square degrees. It is for the same reason, that results show very slight improvement as we increase the coverage capability from 1000 sq. deg. to 3000 sq. deg. We have added an ideal observatory "Best" whose observations are constrained only by the sun. Any pixels outside a 42 ° from the sun is considered as observable in this case. Before we proceed to the discussions let me explain the box and whisker plot with the help of figure 5.3. The results of our simulations are presented using box and whiskers plots. The line in the center of the box represents the median while the star is the mean of the distribution. The lower and upper ends of the box mark that points below which 25 % and 75% of the distribution lies. The difference between the two is statistically referred to as the inter-quartile range (IQR). Whiskers on either side of the box are points where the distribution is 1.5×IQR. Outliers are points which lie outside the whiskers. The box and whiskers plot are used throughout the results section to compare the performance of the locations under inspection. Our interest is to see the distribution and thus the outliers have been in some plots scaled away.

5.2 Observing on Solstices and Equinoxes

As discussed earlier we shift all the events to the day of equinox and compare the probability covered from each site. We break the simulation into two parts – recovery of injected events with a two GW detector network and recoveries with a three GW detector network.

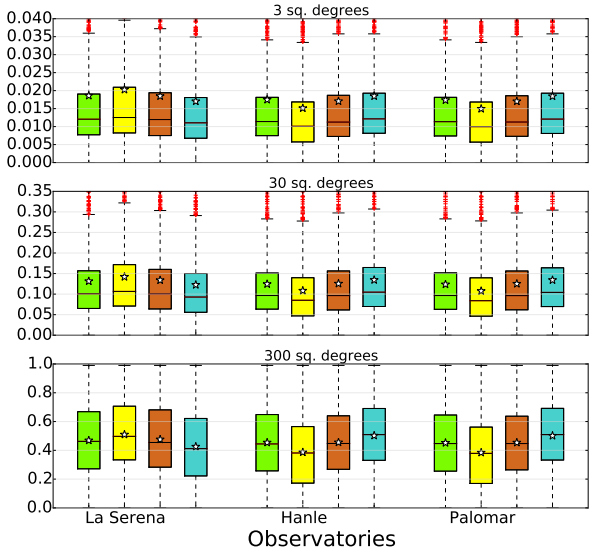

Figure 5.4: Comparing the performance of three locations – La Serena, Hanle and Palomar, after shifting all the injections recovered with a two detector network to the day of vernal equinox (green), summer solstice (yellow), autumn equinox (chocolate) and winter equinox (blue).

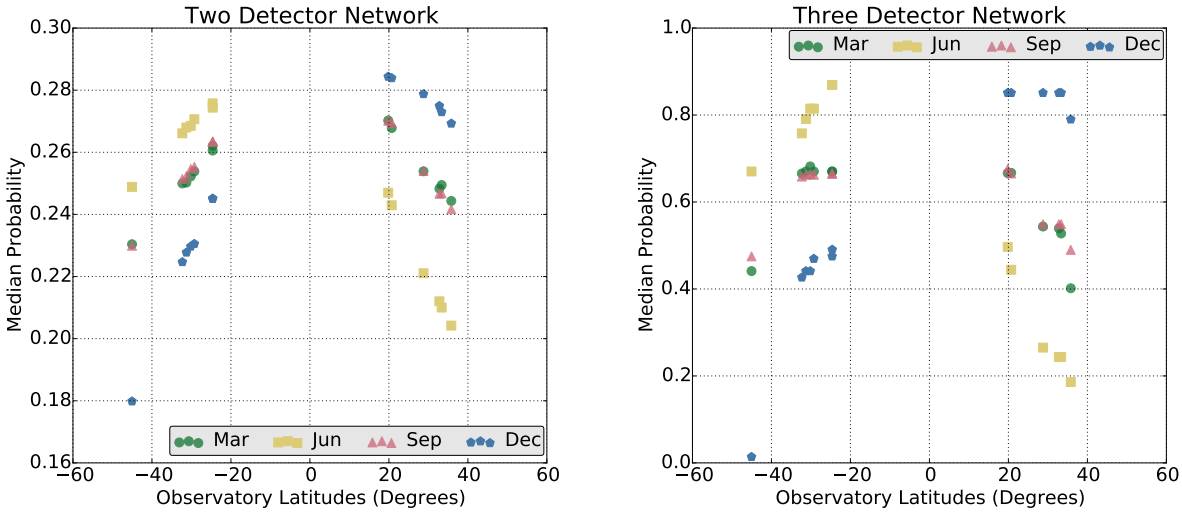

Figure 5.5: We plot the median probability covered by any location when all the injections recovered with a two detector network (left) and with a three detector network (right) are shifted to the day of the vernal equinox (green), summer solstice (yellow), autumn equinox (chocolate) and winter equinox (blue). We see a trend in the median probability covered as a function of the latitude.

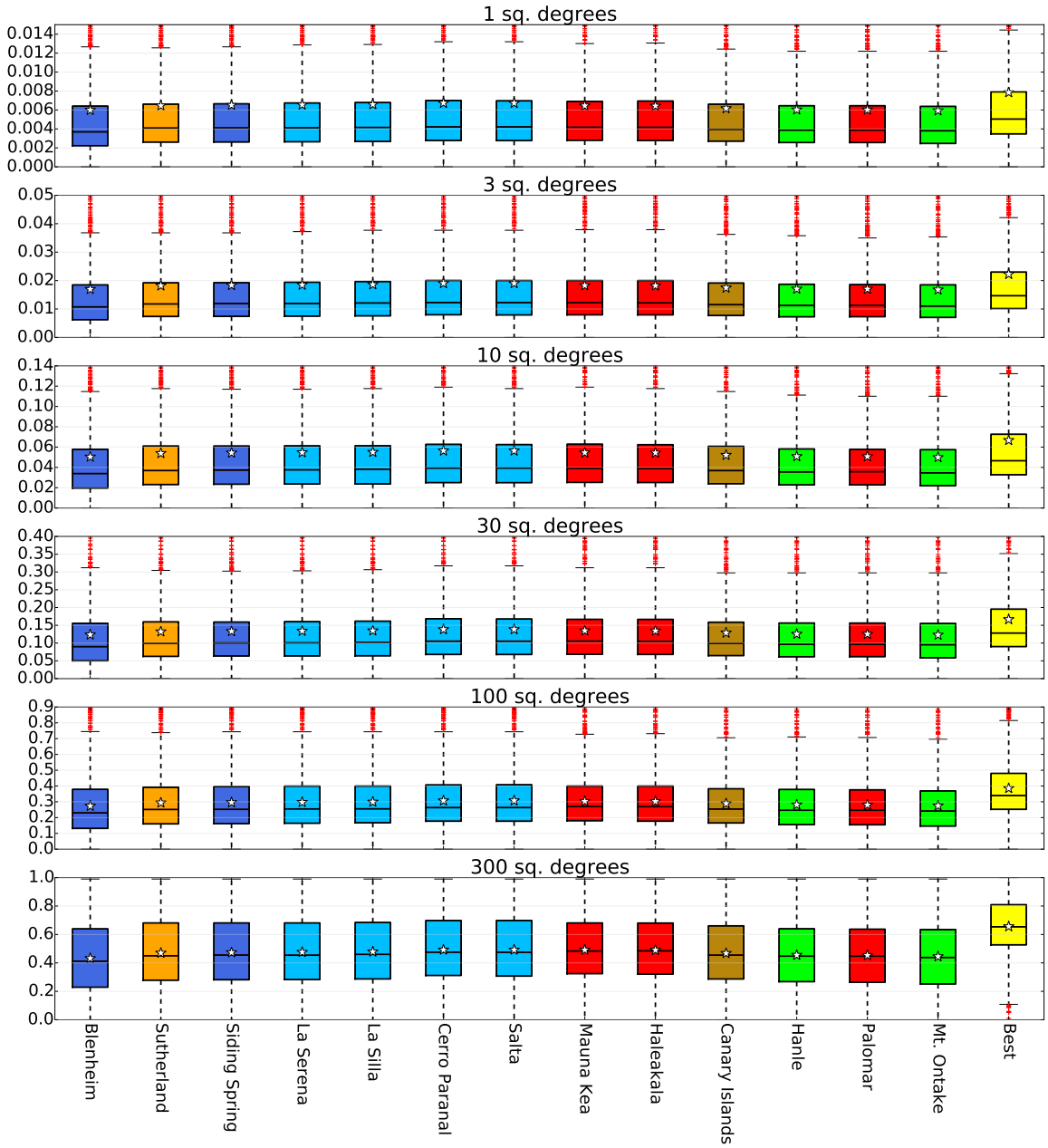

Figure 5.6: The figure compares the location wise performance of all locations when all 1024 events recovered with a two detector network are shifted to the day of the autumn equinox. We see all locations perform comparable with a slight trend in latitude.

For the 1024 patches recovered with a two GW-detector network on the day of autumnal equinox, we observe from figure 5.6 that all sites have comparable performance. The maximum extent of variations across the year for an observatory can be estimated by moving all the injections to the day of summer and winter solstice. One expects that northern hemisphere observatories will outperform the southern on the day the winter solstice and the opposite scenario will occur when all injections are moved to the day of summer solstice. Figure 5.4 supports this hypothesis.

Figure 5.5 shows the probability covered by all the locations under survey, we see an interesting trend when the locations are organized by latitudes. We see that the locations near the mid-latitudes have a higher chance of detecting an EM counterpart as compared to location higher up in latitude – the ones in the temperate zones. The changes across seasons too are less drastic for the former. This discrepancy in performance arises due to two reasons. One, because of the antenna-like sensitivity LIGO detectors, the chances of a source to be detected in the mid-declination is greater than the chance of detecting sources near the equatorial or polar regions. Second, the sites in higher up latitudes have a smaller region of the sky accessible for observation, even on the day of equinox. These factors together explain the trend in performance as a function of latitude.

5.3 LIGO-VIRGO Science Runs

We now shift to more realistic situations. We ask the question how do different locations perform when the detections are distributed over a time interval. We consider the time period of the LIGO O1 run and an example set of dates for the LIGO O2 run. Our results are consistent to changes of dates by $\sim$ 10 days.

We again break the recovered injection into two sets – localization with two GW-detector network and localization with three GW-detector network. The simulation results for 630 events recovered with HL network at O1 sensitivity are shown in figure 5.8. The performance for the 394 events recovered with two detector network but with O2 sensitivity are shown in figure 5.9.

For events recovered with a three GW-detector network, we summarize the location-wise performance with a box and whiskers plot for consistency of representation 5.10. Due to improved localization, we see from figure 5.7, that a large fraction of events are either followed-up to great extent (probability covered >0.95) or could not be followed-up at all (probability covered < 0.05). For a detailed discussion please refer to the published article [22].

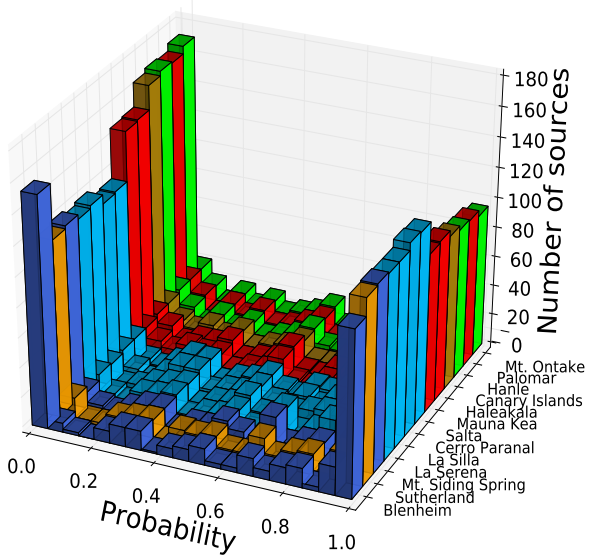

Figure 5.7: Distribution of probability covered when each location is equipped with a 30 sq. deg. coverage capability. We see the performance is limited by the patch visibility and access from any given location as we have a large number of triggers which are covered almost completely $p_{obs} > 0.95$ while other triggers are barely followed-up $p_{obs} < 0.05$.

5.4 Discussion

From the simulations, it is evident that the odds of finding the EM counterparts which evolve on a timescale of a day or longer show a dependence on latitude. Observatories located in the mid-latitudes perform better than the temperate ones. Longitudinal dependence is not seen for the transients evolving on timescales of a day or longer. The seasons have a much larger effect on the performance of an observatory as with seasons the time available to follow-up a localization region changes significantly. The effect of the seasons in follow-up too are relatively harsh in high-latitudes as the length of night changes appreciably. [31] have independently reached similar conclusions by using a different methodology and slightly different assumptions.

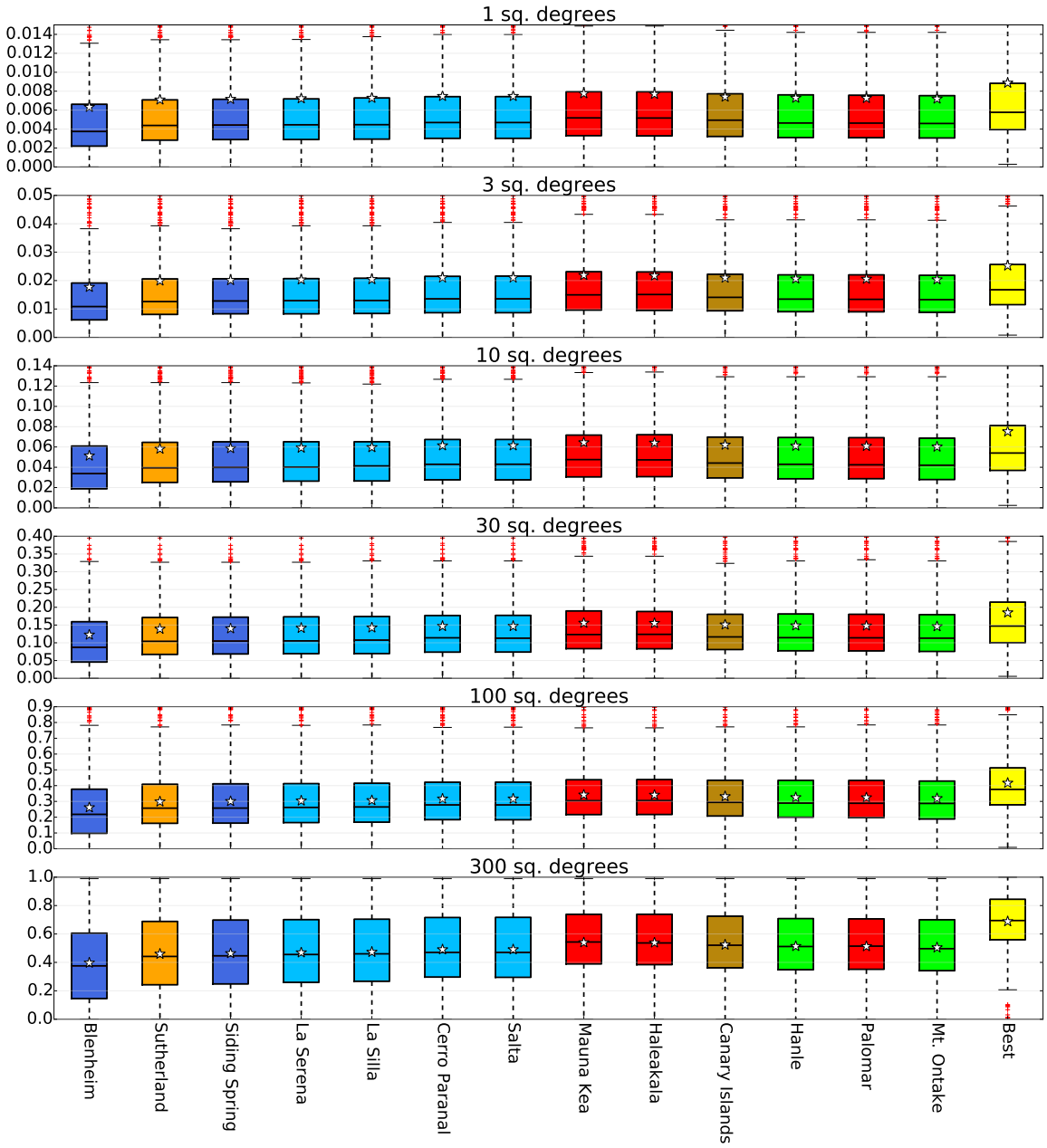

Figure 5.8: Location wise performance for 630 events recovered at O1 detector sensitivity during the O1 observational period.

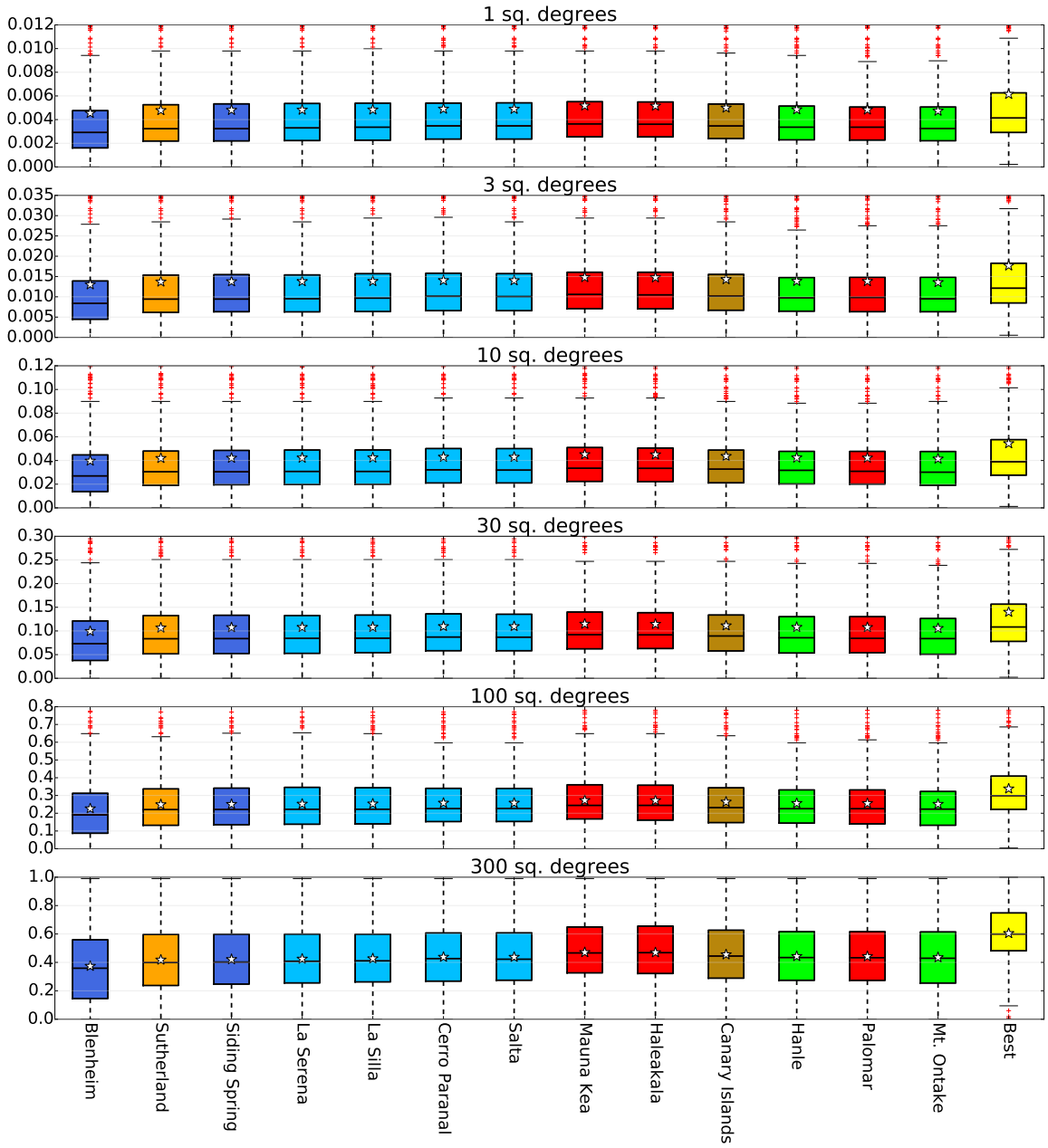

Figure 5.9: Location wise performance for 394 events recovered at O2 detector sensitivity, with events uniformly distributed over the example O2 observational period.

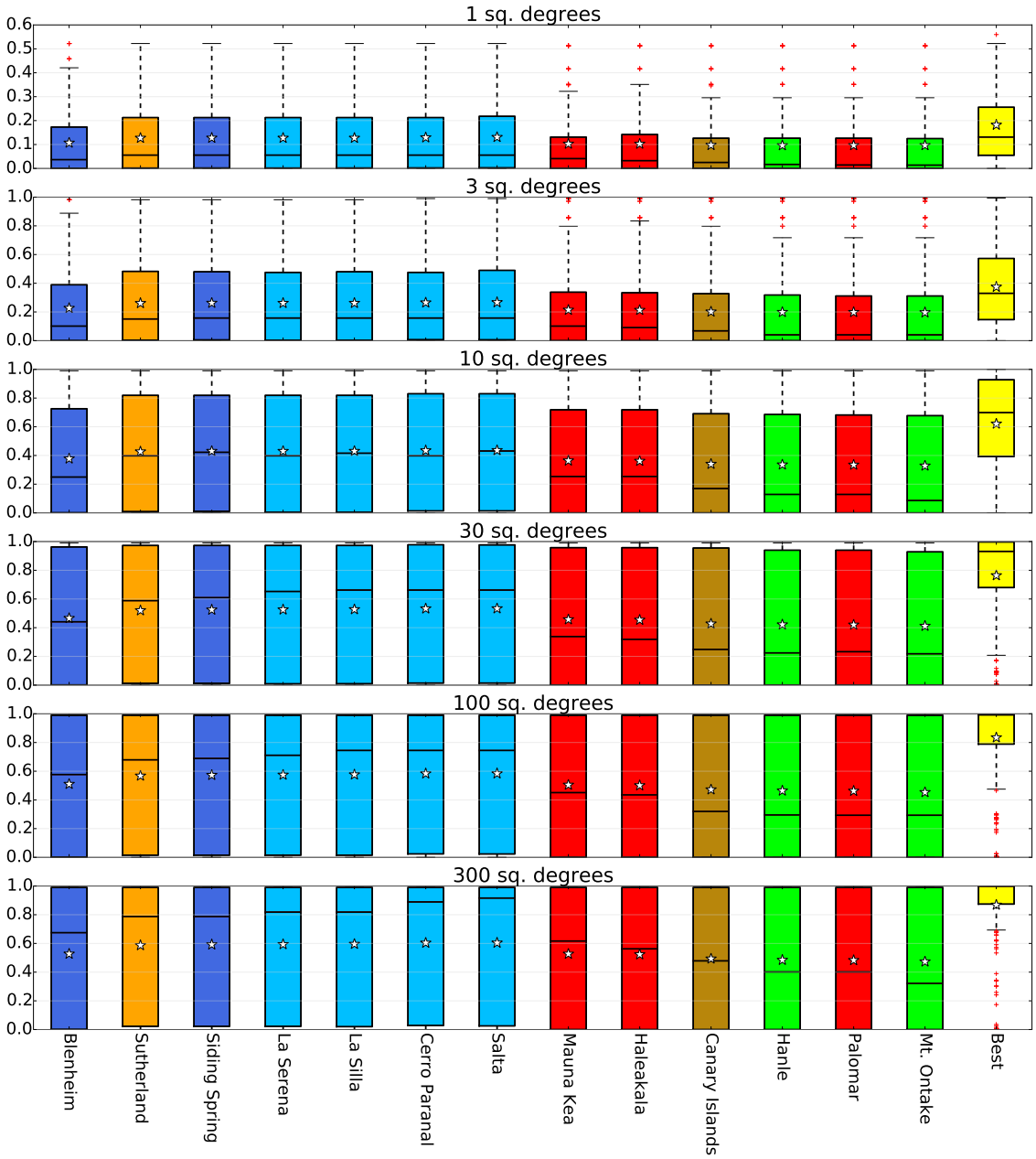

Figure 5.10: Location wise performance for all the events recovered with a three detector network at O2 detector sensitivity. The events are uniformly smeared over the example O2B observational period.

Bibliography

[1] B. D. Metzger and E. Berger. What Is the Most Promising Electromagnetic Counterpart of a Neutron Star Binary Merger? *The Astrophysical Journal*, 746(1):48, 2012.

[2] D. V. Martynov, E. D. Hall, B. P. Abbott, et al. Sensitivity of the Advanced LIGO detectors at the beginning of gravitational wave astronomy. *Physical Review D - Particles, Fields, Gravitation and Cosmology*, 93(11):1–19, 2016.

[3] S Hild. Beyond the second generation of laser-interferometric gravitational wave observatories. *Classical and Quantum Gravity*, 29(12):124006, 2012.

[4] B. P. Abbott, R. Abbott, T. D. Abbott, et al. Prospects for Observing and Localizing Gravitational-Wave Transients with Advanced LIGO and Advanced Virgo. pages 1–35, 2013.

[5] B P Abbott, R Abbott, T D Abbott, et al. Observation of gravitational waves from a binary black hole merger. *Physical Review Letters*, 116(6):1–16, 2016.

[6] B. P. Abbott, R. Abbott, T. D. Abbott, et al. GW151226: Observation of Gravitational Waves from a 22-Solar-Mass Binary Black Hole Coalescence. *Physical Review Letters*, 116(24):1–14, 2016.

[7] B Schutz. *A First Course in General Relativity*. Cambridge University Press, 2009.

[8] B.S. Sathyaprakash and Bernard F Schutz. Physics , Astrophysics and Cosmology with Gravitational Waves arXiv : 0903 . 0338v1 [gr-qc] 2 Mar 2009. *Living Reviews in Relativity*, 12(2), 2009.

[9] The LIGO Scientific Collaboration. Advanced LIGO. *Classical and Quantum Gravity*, 32(7):074001, 2015.

[10] John A. Sidles and Daniel Sigg. Optical torques in suspended Fabry-Perot interferometers. *Physics Letters, Section A: General, Atomic and Solid State Physics*, 354(3):167–172, 2006.

[11] Eiichi Hirose, Keita Kawabe, Daniel Sigg, Rana Adhikari, and Peter R Saulson. Angular instability due to radiation pressure in the LIGO gravitational-wave detector. *Applied optics*, 49(18):3474–3484, 2010.

[12] Matthew Evans, Slawek Gras, Peter Fritschel, et al. Observation of parametric instability in advanced LIGO. *Physical Review Letters*, 114(16):6–9, 2015.

[13] E D Black. An introduction to Pound–Drever–Hall laser frequency stabilization. *American Journal of Physics*, 69(1):79, 2001.

[14] Luc Blanchet. Gravitational Radiation from Post-{N}ewtonian Sources and Inspiralling Compact Binaries. *Living Rev. Relativity*, 5:3, 2002.

[15] J D E Creighton and W G Anderson. *Gravitational-Wave Physics and Astronomy: An Introduction to Theory, Experiment and Data Analysis*. Wiley Series in Cosmology. Wiley, 2012.

[16] James Kennedy and Russell Eberhart. Particle swarm optimization. *Proceedings of ICNN'95 - International Conference on Neural Networks*, pages 1942–1948, 1995.

[17] Yan Wang and Soumya D Mohanty. Particle Swarm Optimization and gravitational wave data analysis: Performance on a binary inspiral testbed. *arXiv.org*, gr-qc:1–14, 2010.

[18] Tito Dal Canton and Others. Implementing a search for aligned-spin neutron star-black hole systems with advanced ground based gravitational wave detectors. *Phys. Rev.*, D90(8):82004, 2014.

[19] Samantha A Usman and Others. The PyCBC search for gravitational waves from compact binary coalescence. *Class. Quant. Grav.*, 33(21):215004, 2016.

[20] Alex Nitz, Ian Harry, Christopher M Biwer, et al. ligo-cbc/pycbc: Test Pre-Release to Validate E@H Travis Build, mar 2017.

[21] Benjamin J. Owen. Search templates for gravitational waves from inspiraling binaries: Choice of template spacing. *Physical Review D*, 53(12):6749–6761, 1996.

[22] Varun Srivastava, Varun Bhalerao, Aravind P. Ravi, Archisman Ghosh, and Sukanta Bose. Geographic and seasonal influences on optical followup of gravitational wave events. 2016.

[23] B. D. Metzger, G. Martínez-Pinedo, S. Darbha, et al. Electromagnetic counterparts of compact object mergers powered by the radioactive decay of r-process nuclei. *Monthly Notices of the Royal Astronomical Society*, 406(4):2650–2662, 2010.

[24] L. F. Roberts, D. Kasen, W. H. Lee, and E. Ramirez-Ruiz. Electromagnetic Transients Powered By Nuclear Decay in the Tidal Tails of Coalescing Compact Binaries. *The Astrophysical Journal*, 736(1):L21, 2011.

[25] S Rosswog, O Korobkin, A Arcones, F Thielemann, and T Piran. The long-term evolution of neutron star merger remnants – I . The impact of r-process nucleosynthesis 1 I N T RO D U C T I O N 2 S I M U L AT I O N S. 756:744–756, 2014.

[26] Masaomi Tanaka, Kenta Hotokezaka, Koutarou Kyutoku, et al. Radioactively Powered Emission From Black Hole-Neutron Star Mergers. 31(3), 2013.

[27] Brian D. Metzger. The Kilonova Handbook. pages 1–62, 2016.

[28] B.˜P. Abbott, R Abbott, T.˜D. Abbott, et al. Supplement: "Localization and Broadband Follow-up of the Gravitational-wave Transient GW150914" (2016, ApJL, 826, L13). *apjs*, 225:8, jul 2016.

[29] Leo P Singer, Larry R Price, Ben Farr, et al. The First Two Years of Electromagnetic Follow-Up with Advanced LIGO and Virgo. *The Astrophysical Journal*, 795(2):105, apr 2014.

[30] Leo P Singer and Larry R Price. Rapid Bayesian position reconstruction for gravitational-wave transients. *Physical Review D*, 93(2):24013, aug 2016.

[31] Hsin-Yu Chen, Reed Essick, Salvatore Vitale, Daniel E Holz, and Erik Katsavounidis. Observational selection effects with ground-based gravitational wave detectors. *LIGO Document*, P1600219:1–7, 2016.